Lidar Assisted Control of Wind Turbines

David Schlipf
Stuttgart Wind Energy, Universität Stuttgart, Allmandring 5B, D-70569 Stuttgart, schlipf@ifb.uni-stuttgart.de

Abstract

LIDAR systems are able to provide preview information of wind speed, direction and shears at various distances in front of the wind turbines. This technology paves the way for new control concepts such as feedforward control and model predictive control to increase the energy production and to reduce loads of wind turbines. This paper describes how the necessary information can be obtained from wind speed measurement provided by a nacelle or spinner based LIDAR system and how this information can be used to improve collective and cyclic pitch control as well as speed and yaw control of wind turbines.

1 Introduction

In recent years LIDAR (Light detection and ranging) technology found its way into wind energy. The possibility to optimize the energy production and reduce the fatigue and extreme loads by nacelle or spinner based LIDAR systems is an important issue. The presented work describes how wind characteristics, such as wind speed, direction and shears, can be reconstructed from the limited provided information and how this information can be used in different applications. The strategies are tested using full turbulent wind fields and an aeroelastic simulation model of a $5\,\mathrm{MW}$ wind turbine. The wind information is obtained by simulating a LIDAR system with the LIDAR simulator presented in [1].

The work focuses on LIDAR assisted feedforward collective pitch using the knowledge of the incoming wind speed providing an additional control update to assist common collective pitch control. Traditionally, the rotor speed is adjusted by changing the blade pitch angle depending on the rotor speed itself. Due to the inertia of the rotor, the speed adaptation to the changing inflow conditions is delayed. Additional load reduction compared to a sophisticated feedback controller can be archived [2]. The core of this controller is an adaptive filter accounting for not perfect LIDAR measurements and wind evolution.

Then the theoretical potential to increase the energy production by tracking optimal inflow conditions is presented. A predictive feed forward control strategy is proposed to exploit the benefit of the knowledge of the incoming wind. The comparison to existing indirect speed control strategies shows a marginal increase in energy output at the expense of raised fluctuations of the generator torque [3].

A Nonlinear Model Predictive Control (NMPC) is also presented, which predicts and optimizes the future behavior of a wind turbine using the wind speed preview adjusting simultaneously the pitch angle and the generator torque. The multi variable nature of the NMPC allows to archive further load reductions especially for for wind conditions near rated wind speed [4].

Furthermore, an cyclic pitch feedforward controller using the measured horizontal and vertical shear is introduced to assist common cyclic pitch control for further reduction of blade loads. Results from simulations ([5], [6]) are promising, but they have to be further investigated under more realistic conditions.

Finally, the benefit of LIDAR assisted yaw control is explored. Traditionally, the wind direction signal is measured at one single disturbed point behind the blades. A promising way to obtain a more accurate measurement of the incoming wind direction is to measure it over the full rotor plane ahead of the turbine by LIDAR. To evaluate the benefit in energy output, measurements from a nacelle sonic anemometer are compared to a scanning LIDAR system installed on a $5\,\mathrm{MW}$ turbine [7]. The expected increase of the energy output is about one percent of the annual energy production, when using the wind direction signal from the LIDAR system instead of the sonic anemometer [3].

This paper is organized as follows: Section 2 deals with the wind field reconstruction based on line-of-sight wind speeds and simulations of LIDAR measurements. In Section 2 to 6 the different control concepts are presented. Section 7 concludes the paper.

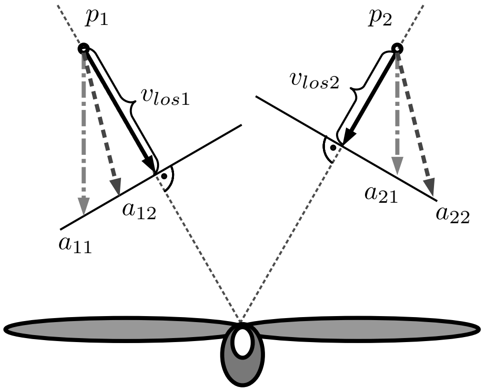

Figure 1: Ambiguity in wind reconstruction.

2 Wind Reconstruction and LIDAR simulations

To be able to use LIDAR measurements in turbine control they first have to be analyzed. In this section a method is proposed to retrieve the necessary information for LIDAR assisted control from nacelle or spinner based LIDAR measurements. First the ambiguity in wind reconstruction is presented. Then LIDAR and wind models are introduced to which can be applied to reconstruct wind characteristics. Finally a more detailed LIDAR model used for simulation is described. Further details can be found in [3].

2.1 The Cyclops Dilemma

LIDAR systems are able to measure the speed of aerosols by the Doppler shift in the frequency of backscattered light. The limitation to the line-of-sight direction causes a problem using a single nacelle or spinner based LIDAR system for wind turbine control. This effect we called the "Cyclops dilemma": As a Cyclops cannot see three-dimensionally with only one eye, it is not possible to measure a three-dimensional wind vector by only one LIDAR system. For reconstruction of the three dimensional wind vector, three LIDAR systems focusing on the same point with linearly independent laser beams are needed, as used in the Musketeer experiment [8]. Using only one nacelle or spinner mounted LIDAR system, the two missing systems can be omitted by using e.g. one of the following two assumptions:

1. no vertical and no horizontal wind component
2. no vertical component and homogeneous flow

In Figure 1 the effect of both assumptions is shown. In this case the 3D vectors in the location p_1 and p_2 (measured at the same height) should be reconstructed from the line-of-sight wind speeds $v_{los,1}$ and $v_{los,2}$. The first assumption yields a_{11} and a_{21} representing a horizontal shear. By the second assumption the resulting vectors a_{12} and a_{22} are equal representing a cross-flow, as homogeneous flow on each height was assumed.

The dilemma exists, as long as the LIDAR measurement is used for yaw and pitch control at the same time: If the first assumption is used to calculate the inhomogeneous inflow, perfect alignment is assumed. If the second assumption is used to obtain the misalignment, homogeneous flow is assumed.

Nevertheless, nacelle or spinner based LIDAR systems can provide a good estimate of wind characteristics such as wind speed, shear and wind direction, depending on the used assumptions. Those assumptions will be used to derive internal reduced wind and LIDAR models. These models can be used in an estimator and have to be designed depending on the application. The estimator will give a perfect estimation of the wind characteristics, if the simulation model coincide with the internal model. Depending on the robustness, the estimated values will differ from the real ones using real data or more complex simulations. This method will be explained in the remainder of this section.

2.2 Model of the LIDAR Measurements for Reconstruction

In a first step it is important to understand the problem introduced by the measurement technique. The LIDAR measurement of line-of-sight wind speed $v_{los,i}$ of each focus point $\begin{bmatrix} x_i & y_i & z_i \end{bmatrix}^T$ can be modeled by

$$v_{los,i} = l_{xi}u_i + l_{yi}v_i + l_{zi}w_i, \tag{1}$$

which is the projection of the wind vector $\begin{bmatrix} u_i & v_i & w_i \end{bmatrix}^T$ in the ith focus point on the normalized laser beam vector with focus length f_i:

$$\begin{bmatrix} l_{xi} \\ l_{yi} \\ l_{zi} \end{bmatrix} = \frac{1}{f_i} \begin{bmatrix} x_i \\ y_i \\ z_i \end{bmatrix}. \tag{2}$$

This equation shows how information is lost: For each measurement this model gives one equation with 3 unknowns (u_i, v_i, w_i) and therefore cannot be solved. By using three LIDAR systems focusing from linearly independent directions at the same focus point two equations can be added without new unknowns and the wind vector can be reconstructed with a unique solution.

2.3 Wind Reconstruction Models

The LIDAR measurement models (1) and (2) can be combined with different wind construction model which has to be chosen according to the application.

2.3.1 Wind Reconstruction Model v_0

The simplest model assumes that only the rotor effective wind is present and no shears or inflow angles. In this case the u_i component is equal to the rotor effective wind, the v_i and w_i are 0:

$$\begin{bmatrix} u_i \\ v_i \\ w_i \end{bmatrix} = \begin{bmatrix} v_0 \\ 0 \\ 0 \end{bmatrix}. \tag{3}$$

Using (1) yield:

$$v_{los,i} = l_{xi}u_i. \tag{4}$$

For n_{fp} focus points measured in the same vertical measurement plane in front of the turbine ($x_i = x \forall i$), the rotor effective wind can be defined as:

$$v_0 = \frac{1}{n_{fp}} \sum_{i}^{n} u_i / l_{xi}. \tag{5}$$

2.3.2 Wind Reconstruction Model v_0-δ_H-δ_V

In the second model, the wind direction is known and it is assumed that the wind is homogeneous in a vertical measurement plane in front of the turbine ($x_i = x \forall i$). If there is no tilted inflow α_V and no misalignment α_H the turbulent wind vector field is reduced to

$$\begin{bmatrix} u_i \\ v_i \\ w_i \end{bmatrix} = \begin{bmatrix} v_0 + \delta_H y_i + \delta_V z_i \\ 0 \\ 0 \end{bmatrix}. \tag{6}$$

Following unknown wind characteristics are used: v_0 is the effective wind speed and δ_H and δ_V are the horizontal and vertical shear, respectively.

The advantage of this reduction is that n_{fp} measurements gathered simultaneously in the same measurement plane can be combined to get an estimation for the rotor effective wind characteristics. For non simultaneous measurements of scanning LIDAR systems, the last n_{fp} focus points of a scan can be used. In both cases the focus points should be well distributed. For the combination of different measurement planes, e.g. by a pulsed system, see Section 2.4.

If, for example, it is assumed, that there is no tilted inflow and no misalignment ($\alpha_V = \alpha_H = 0$), following equations are obtained using (6), (1) and (2):

$$\underbrace{\begin{bmatrix} f_1 v_{los,1} \\ \vdots \\ f_{n_{fp}} v_{los,n_{fp}} \end{bmatrix}}_{m} = \underbrace{\begin{bmatrix} x & xy_1 & xz_1 \\ \vdots & \vdots & \vdots \\ x & xy_{n_{fp}} & xz_{n_{fp}} \end{bmatrix}}_{A} \underbrace{\begin{bmatrix} v_0 \\ \delta_H \\ \delta_V \end{bmatrix}}_{s}. \tag{7}$$

A solution for all three wind characteristics can only be found, if $rank(A) = 3$. If all measurements are obtained in one straight line, this condition is not fulfilled. For $n_{fp} = 3$ there is one unique solution

$$s = A^{-1}m. \tag{8}$$

For $n_{fp} > 3$ a solution can be selected by the method of least squares. If for example δ_H or δ_V is set to zero, because is assumed that there is no horizontal shear, there is no impact to the estimation of the other two unknowns. In a similar way a model v_0-α_H-α_V can be derived.

2.3.3 Wind Reconstruction Model v_0-α_H

This model assumes that there is no shear and no tilted inflow and that the wind speed v_0 and the misalignment α_H are the same.

$$\begin{bmatrix} u_i \\ v_i \\ w_i \end{bmatrix} = \begin{bmatrix} u \\ v \\ w \end{bmatrix} = \begin{bmatrix} v_0 \cos\alpha_H \\ v_0 \sin\alpha_H \\ 0 \end{bmatrix}. \tag{9}$$

Using (9), (1) and (2) a linear system in u and v can be formulated:

$$\underbrace{\begin{bmatrix} f_1 v_{los,1} \\ \vdots \\ \vdots \\ f_{n_{fp}} v_{los,n_{fp}} \end{bmatrix}}_{m} = \underbrace{\begin{bmatrix} x & y_1 \\ \vdots & \vdots \\ \vdots & \vdots \\ x & y_{n_{fp}} \end{bmatrix}}_{A} \underbrace{\begin{bmatrix} u \\ v \end{bmatrix}}_{s}. \tag{10}$$

This system can be solved using the estimator (8), if $rank(A) = 2$. The wind characteristics can be calculated:

$$\begin{aligned} v_0 &= \sqrt{s_1^2 + s_2^2} \\ \alpha_H &= \arctan\frac{s_1}{s_2}, \end{aligned} \tag{11}$$

with s_i the ith component of s.

The proposed model is validated with measurement data where a lidar scanner was installed on the nacelle of a stopped wind turbine with a hub height of 34 m at the Risø-DTU test site [9]. The lidar system points to a met mast equipped with several ultrasonic anemometers. Figure 2 shows the reconstruction methods of the u and v component yield good correlations.

2.3.4 Wind Reconstruction Model v_0-α_H-δ_V

The next model takes the unknown misalignment α_H of the turbine and the unkown verical shear δ_V in consideration and assumes that there is no horizontal shear and no tilted inflow:

$$\begin{bmatrix} u_i \\ v_i \\ w_i \end{bmatrix} = \begin{bmatrix} \cos\alpha_H (v_0 + \delta_V z_i) \\ \sin\alpha_H (v_0 + \delta_V z_i) \\ 0 \end{bmatrix}. \tag{12}$$

Using (12), (1) and (2) a nonlinear equation system in v_0, α_H and δ_V is obtained, but similar to (7) a linear system in s can be formulated:

$$\underbrace{\begin{bmatrix} f_1 v_{los,1} \\ \vdots \\ \vdots \\ f_n v_{los,n_{fp}} \end{bmatrix}}_{m} = \underbrace{\begin{bmatrix} x & xz_1 & y_1 & y_1 z_1 \\ \vdots & \vdots & \vdots & \vdots \\ \vdots & \vdots & \vdots & \vdots \\ x & xz_{n_{fp}} & y_{n_{fp}} & y_n z_{n_{fp}} \end{bmatrix}}_{A} \underbrace{\begin{bmatrix} v_0 \cos\alpha_H \\ \delta_V \cos\alpha_H \\ v_0 \sin\alpha_H \\ \delta_V \sin\alpha_H \end{bmatrix}}_{s}. \tag{13}$$

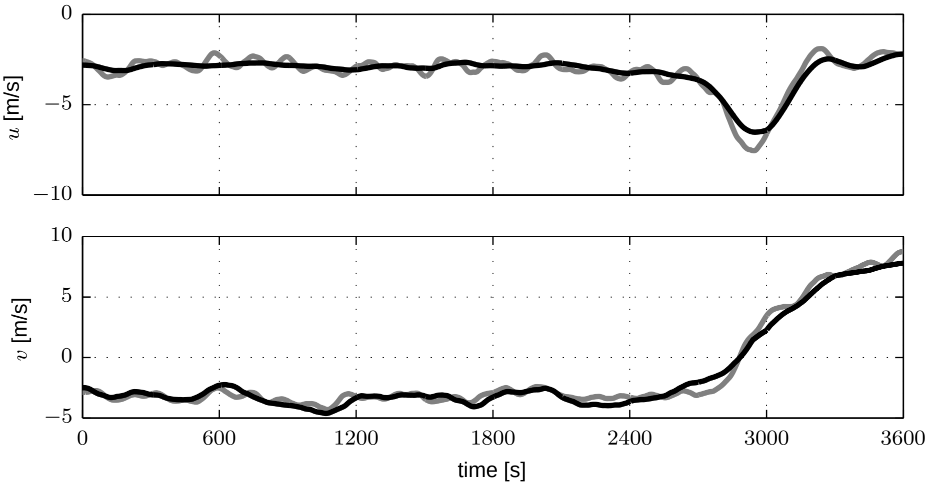

Figure 2: Comparison of longitudinal and lateral wind speed (1 min average) from sonic (gray) and reconstructed from lidar data (black).

This system can be solved using the estimator (8), if $rank(A) = 4$. The wind characteristics can be calculated:

$$\begin{aligned} v_0 &= \sqrt{s_1^2 + s_3^2} \\ \alpha_H &= \arctan \frac{s_1}{s_3} \\ \delta_V &= \sqrt{s_2^2 + s_4^2}, \end{aligned} \tag{14}$$

with s_i the ith component of s. In the same way a model v_0-α_V-δ_H can be defined.

2.3.5 Problems of Wind Reconstruction Model v_0-α_H-δ_H

Instead of, or in addition to δ_V, the horizontal shear can be included in the wind model (12):

$$\begin{bmatrix} u_i \\ v_i \\ w_i \end{bmatrix} = \begin{bmatrix} \cos\alpha_H(v_0 + \delta_H y_i) \\ \sin\alpha_H(v_0 + \delta_H y_i) \\ 0 \end{bmatrix}. \tag{15}$$

But when combining (15), (1) and (2) one obtains:

$$\underbrace{\begin{bmatrix} f_1 v_{los,1} \\ : \\ : \\ f_n v_{los,n_{fp}} \end{bmatrix}}_{m} = \underbrace{\begin{bmatrix} x & xy_1 & y_1 & y_1 y_1 \\ : & : & : & : \\ : & : & : & : \\ x & xy_{n_{fp}} & y_{n_{fp}} & y_{n_{fp}} y_{n_{fp}} \end{bmatrix}}_{A} \underbrace{\begin{bmatrix} v_0 \cos\alpha_H \\ \delta_V \cos\alpha_H \\ v_0 \sin\alpha_H \\ \delta_V \sin\alpha_H \end{bmatrix}}_{s}. \tag{16}$$

Due to the same x component, the second and third column are linear dependent ($rank(A) \leq 3$) and therefore α_H and δ_H cannot be estimated with the estimator (8). With a pulsed LIDAR system, it is possible to avoid this problem by measuring in different planes in front of the turbine and by combining those measurements, but this is beyond the scope of this work. The presented problem also holds for a model v_0-α_V-δ_V.

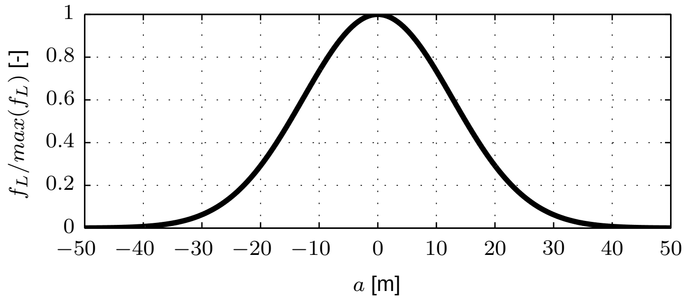

Figure 3: Normalized range weighing function $f_L(a)$ for a pulsed LIDAR system.

2.4 Simulated LIDAR Measurements and Reconstruction

LIDAR systems need to be simulated to test LIDAR assisted controller. The model (1) is very simplified due to the volume measurement of real LIDAR systems. The line-of-sight wind speed can be modeled more realistically by the following equation:

$$v_{los,i} = \int_{-\infty}^{\infty} (l_{xi}u(a) + l_{yi}v(a) + l_{zi}w(a))f_L(a)da. \tag{17}$$

The weighting function $f_L(a)$ at the distance a to the focus point depends on the used LIDAR technology (pulsed or continuous wave). For the simulation in Section 4 to 7 a Gaussian shape weighting function with full width at half maximum (FWHM) of $W = 30\ \mathrm{m}$ is used, see Figure 3, following the considerations of [10] and [11]:

$$f_L(a) = \frac{e^{-4\ln 2(a/W)^2}}{\int_{-\infty}^{\infty} e^{-4\ln 2(a/W)^2}da} = \frac{2\ln 2e^{-4\ln 2(a/W)^2}}{W\sqrt{\ln 2\pi}}. \tag{18}$$

3D Wind fields generated e.g. with TurbSim [12] over time t and the coordinates y and z can be scanned at a trajectory point $[t_i, x_i, y_i, z_i]$ by assuming Taylor's Hypothesis of Frozen Turbulence. The x_i coordinate is transformed with the mean wind speed $\bar{u}$ to

$$T_{\text{Taylor}} = x_i/\bar{u}. \tag{19}$$

The 3D wind fields can then be evaluated at $t_i + T_{\text{Taylor}}$. In this work a pulsed system with a circular trajectory is used, which is performed within $T_t = 2.4\ \mathrm{s}$ with 12 focus points in 5 focus distances equally distributed between $0.5D$ and $1.5D$ with the rotor diameter $D = 126\ \mathrm{m}$, resulting in a update rate of $\Delta t_L = 0.2\ \mathrm{s}$, see Figure 4. This trajectory was realized by a real scanning LIDAR system installed on the nacelle of a $5\ \mathrm{MW}$ turbine (see [7]). In the simulation, effects such as collision of the laser beam with the blades, volume measurement and mechanical constraints of the scanner from data of the experiment are considered to obtain realistic measurements. The wind characteristics are then reconstructed using 4, extended for pulsed LIDAR systems with several measurement distances: For each distance i the longitudinal wind component is averaged over the last trajectory for a rotor effective value and the obtained time series of the measurements v_i is time-shifted according to Taylor's frozen turbulence hypothesis. The preview time is then $T_{\text{Taylor},i}$ reduced by the time shift due to the running average of half of the trajectory duration T_t, see Figure 5. The rotor effective wind speed $v_0(t)$ is then calculated by

$$v_0(t) = \frac{1}{5}\sum_{i=1}^{5} v_i(t - T_{\text{Preview},i}). \tag{20}$$

This improves the short term estimation, because the measurements of further distances can be stored and used to obtain more information when reaching the nearest distance. If there is no measurement available for the first focus distance, the average is made only over the last four distances and so on.

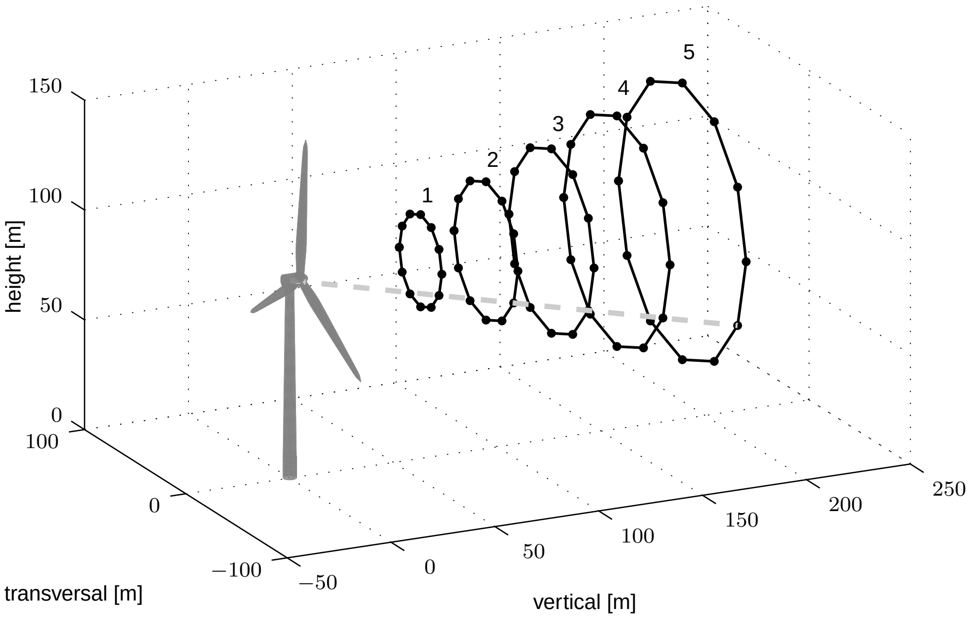

Figure 4: Simulated LIDAR system performing a circular trajectory.

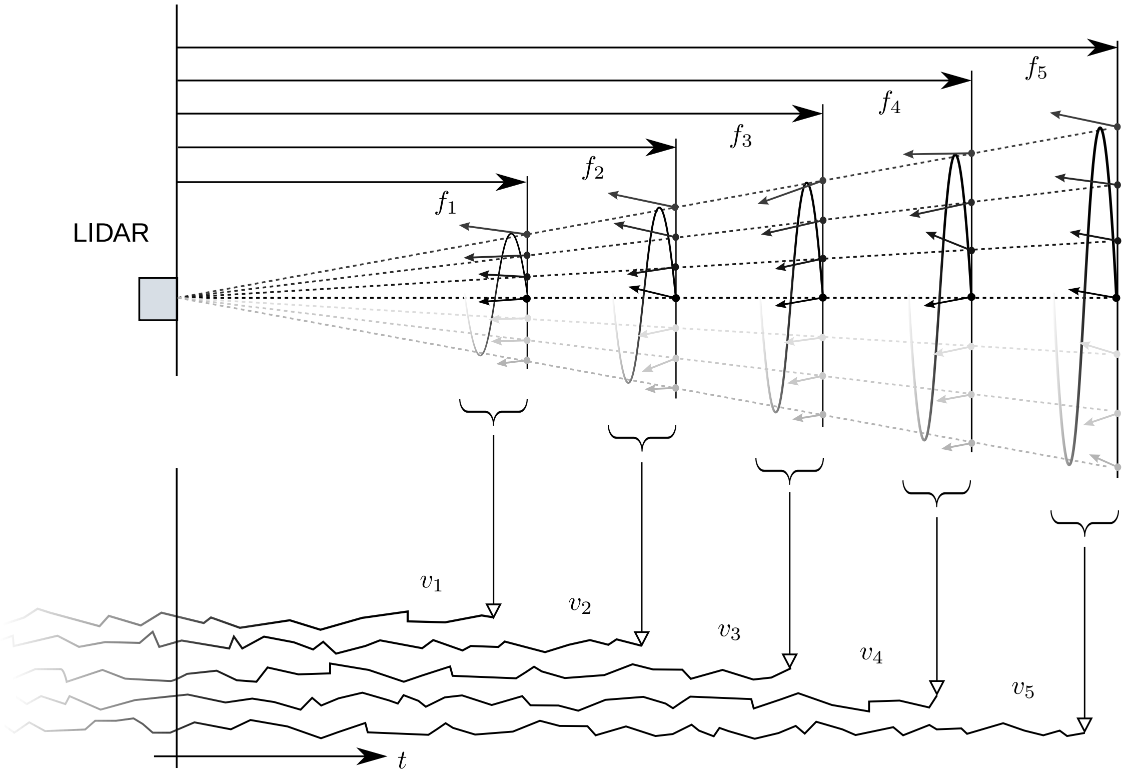

Figure 5: Scope of the wind prediction: The line-of-sight wind speeds are measured at different fixed distances, corrected and averaged over the last trajectory. The resulting preview of the rotor effective wind speed $v_0(t)$ is a weighted average over all available v_i.

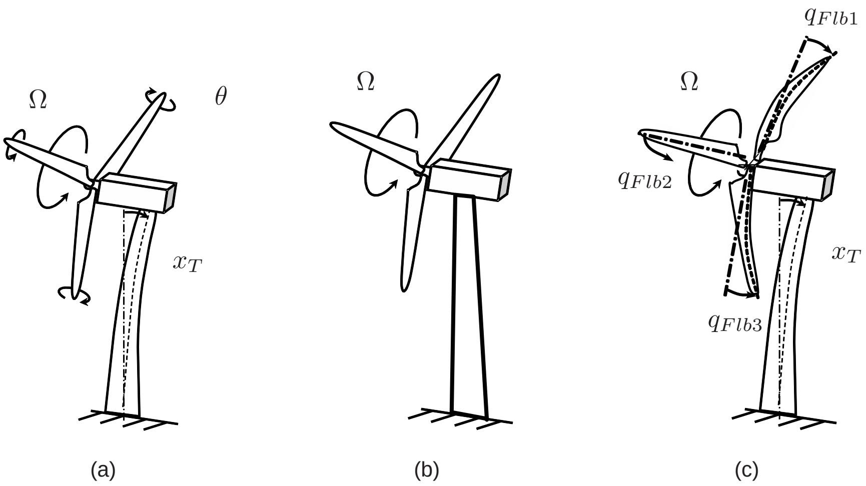

Figure 6: Degrees of freedom for the reduced nonlinear model (a), the first order model (b) and the linear model (c).

3 Modeling of the Wind Turbine

The crucial part of a successful feedforward and model predictive controller design is the adequate modeling of the dynamic system to be controlled. The model should be simple enough to allow a partial system inversion (for the feedforward controller design) and simulations in reasonable computation time (for the NMPC) and at the same time it should be accurate enough to capture the system dynamics that are relevant for the wind turbine control. The reduced model can be also used in an estimator to estimate the rotor effective wind speed from turbine data.

3.1 Reduced Nonlinear Model

Classically aeroelastic simulation environments for wind turbines such as FAST [13] (used later in this work), provide models close to reality but far to complex to be used for controller design. In addition, current remote sensing methods such as LIDAR are not able to provide a wind field estimate with comparable details to a generic wind field used by aeroelastic simulations (generated in this work with TurbSim [12]). In this section a turbine model with three degrees of freedom (see Figure 6(a)) is derived from physical fundamentals and the wind field is reduced to the rotor effective wind speed which is measurable with existing LIDAR technology.

The first tower fore-aft bending mode, the rotational motion and the collective pitch actuator are based on [14]:

$$J\dot{\Omega} + M_g/i = M_a(\dot{x}_T, \Omega, \theta, v_0) \tag{21a}$$

$$m_{Te}\ddot{x}_T + c_T\dot{x}_T + k_T x_T = F_a(\dot{x}_T, \Omega, \theta, v_0) \tag{21b}$$

$$\ddot{\theta} + 2\xi\omega\dot{\theta} + \omega^2(\theta - \theta_c) = 0. \tag{21c}$$

Equation (21a) models the drive-train dynamics, where Ω is the rotor speed, M_a is the aerodynamic torque and M_g the electrical generator torque, x_T the tower top fore-aft displacement, θ the effective collective blade pitch angle, and v_0 the rotor effective wind speed. Moreover, i is the gear box ratio and J is the sum of the moments of inertia about the rotation axis of the rotor hub, blades and the electric generator. Equation (21b) describes the tower fore-aft dynamics, F_a is the aerodynamic thrust and m_{Te}, c_T, and k_T are the tower equivalent modal mass, structural damping and bending stiffness, respectively. These values were calculated according to [15] and [16]. Finally, equation (21c) is a second-order model of the blade pitch actuator, where ω is the undamped natural frequency and ξ the damping factor of the pitch actuator and θ_c is the collective blade pitch control input.

The nonlinearity in the reduced model resides in the aerodynamic thrust and torque acting on the rotor with the radius R:

$$M_a(\dot{x}_T,\Omega,\theta,v_0) = \frac{1}{2}\rho\pi R^3 \frac{c_P(\lambda,\theta)}{\lambda} v_{rel}^2 \tag{22a}$$

$$F_a(\dot{x}_T,\Omega,\theta,v_0) = \frac{1}{2}\rho\pi R^2 c_T(\lambda,\theta) v_{rel}^2, \tag{22b}$$

where ρ is the air density, λ the tip-speed ratio, defined as

$$\lambda = \frac{\Omega R}{v_{rel}}, \tag{23}$$

and c_P and c_T are the effective power and thrust coefficients, respectively. The nonlinear c_P and c_T coefficients can be obtained from steady state simulation.
The relative wind speed v_{rel} is defined as a superposition of tower top speed and mean wind speed

$$v_{rel} = (v_0 - \dot{x}_T), \tag{24}$$

and is used to model the aerodynamic damping. The equations (21) to (24) can be organized in the usual nonlinear state space form:

$$\begin{aligned} \dot{x} &= f(x,u,d) \\ y &= h(x,u,d), \end{aligned} \tag{25}$$

where the system states x, the system inputs u, disturbance d and measurable outputs y are

$$\begin{aligned} x &= \begin{bmatrix} \Omega & x_T & \dot{x}_T & \theta & \dot{\theta} \end{bmatrix}^T \\ u &= \begin{bmatrix} M_g & \theta_c \end{bmatrix}^T \\ d &= v_0 \\ y &= \begin{bmatrix} \Omega & \ddot{x}_T & \theta & \dot{\theta} \end{bmatrix}^T. \end{aligned} \tag{26}$$

3.2 Estimation of the Rotor Effective Wind Speed from Turbine Data

The nonlinear reduced model (21) can be further reduced to a first order system (see Figure 6(b)) by ignoring the tower movement and the pitch actuator:

$$J\dot{\Omega} + M_g/i = M_a(\Omega,\theta,v_0) \tag{27a}$$

$$M_a(\Omega,\theta,v_0) = \frac{1}{2}\rho\pi R^3 \frac{c_P(\lambda,\theta)}{\lambda} v_0^2 \tag{27b}$$

$$\lambda = \frac{\Omega R}{v_0}. \tag{27c}$$

This model is used to estimate the rotor effective wind speed v_0 from turbine data. If parameter such as inertia J, gear box ratio i and rotor radius R as well es the power coefficient $c_P(\lambda,\theta)$ are known, and data such as generator torque M_g, pitch angle θ, rotor speed Ω and air density ρ is measurable, the only unknown in (27) is the rotor effective wind v_0.
Due to the λ-dependency of the power coefficient $c_P(\lambda,\theta)$ no explicit solution can be found. A solution could be found by solving the (27) by iterations. But this would produce high computational effort for high resolution data. Therefore a three dimensional look-up-table $v_0(M_a,\Omega,\theta)$ is calculated a priori from the cubic equation (27b), similar to [17]. Here the equation (27b) in solved first in λ for numerical reasons. The aerodynamic torque M_a can then be calculated on line from turbine data with (27a).

3.3 Linear Model

For the cyclic pitch feedforward controller (see Section 7), a model including the blade bending degree of freedom is needed. It is obtained from an azimuth dependent nonlinear aeroelastic model considering the rotor motion, first flapwise bending modes of each blade and the first tower fore-aft bending mode as depicted in Figure 6(c). The aeroelastic model is linearized, transformed with the Coleman-Transformation and decoupled, details see [18].

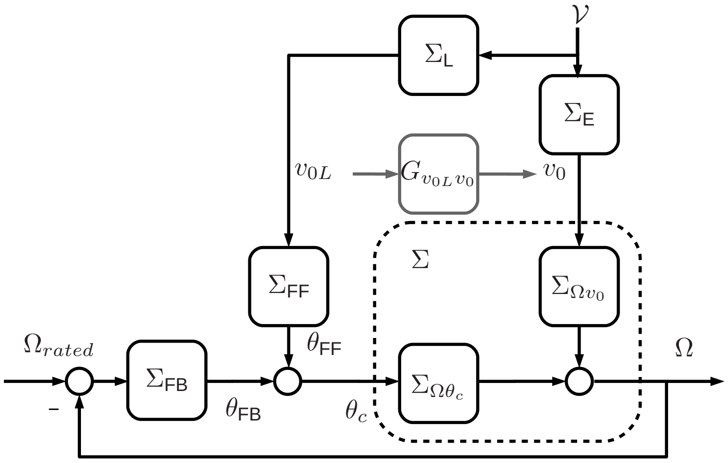

Figure 7: Feedforward control: The feedforward controller Σ_{FF} tries to compensate the effects of the wind field $\mathcal{V}$ to the rotor speed Ω.

4 LIDAR Assisted Collective Pitch Control

The collective pitch feedforward controller (see Figure 7) is based on the work in [2] and combines the baseline feedback controller with a feedforward update. The main control goal of the collective pitch feedback controller Σ_{FB} is to maintain the rated rotor speed Ω_{rated}. The system Σ is disturbed by a wind field $\mathcal{V}$, which can be measured by a LIDAR system Σ_{L} in front of the turbine before reaching the rotor. If the wind would not change on its way ($\Sigma_{\mathsf{E}} = 1$) and in the case of perfect measurement the measured wind speed v_{0L} and the rotor effective wind speed v_0 are equal. The disturbance could be perfectly compensated by a feedforward controller $\Sigma_{\mathsf{FF}} = -\Sigma_{\Omega\theta_c}^{-1}\,\Sigma_{\Omega v_0}$, if the influence on the generator speed of the wind $\Sigma_{\Omega v_0}$ and the pitch angle $\Sigma_{\Omega\theta_c}$ is known and $\Sigma_{\Omega\theta_c}$ is invertible.
In reality v_0 cannot be measured perfectly due to the limitation of the LIDAR system and Σ_{E} is quite complex to model. However, if the transfer function $G_{v_{0L}v_0}$ from the measured wind speed to the rotor effective wind speed is known, the following feedforward controller compensates all the disturbances:

$$\Sigma_{\mathsf{FF}} = -\Sigma_{\Omega\theta_c}^{-1}\,\Sigma_{\Omega v_0}\,G_{v_{0L}v_0}. \tag{28}$$

Due to its complexity this perfect compensation cannot be found for an aeroelastic model, but for the reduced nonlinear model presented above. With the stationary pitch curve $\theta_{ss}(v_{0ss})$, which can be obtained from simulations or measurements, the part $-\Sigma_{\Omega\theta_c}^{-1}\,\Sigma_{\Omega v_0}$ is:

$$\theta_{\mathsf{FF}} = \theta_{ss}((\ddot{v}_{0L} + 2\xi\omega\dot{v}_{0L} + \omega^2 v_{0L})/\omega^2). \tag{29}$$

This controller is not proper but is well defined because of the LIDAR preview.
The transfer function $G_{v_{0L}v_0}$ is modeled by

$$G_{v_{0L}v_0} = |G_{v_{0L}v_0}|e^{T_{\mathsf{Preview}}s}, \tag{30}$$

where T_{Preview} is the preview time of the LIDAR due to Taylor's Hypothesis. The magnitude can be analytically modeled or estimated from simulated or measured data via the auto spectrum of the measured wind speed $S_{v_{0L}v_{0L}}$ and the cross spectrum $S_{v_0v_{0L}}$ between the measured and the rotor effective wind speed:

$$|G_{v_{0L}v_0}| = \frac{|S_{v_0v_{0L}}|}{|S_{v_{0L}v_{0L}}|}. \tag{31}$$

Figure 30 shows $|G_{v_{0L}v_0}|$ for a $1\,\mathrm{h}$ simulation with mean wind speed $\bar{v} = 16\,\mathrm{m/s}$ and a turbulence intensity of 18% not over the frequency f as used commonly, but over the wavenumber $k = 2\pi f/\bar{v}$. Due to the Kaimal wind spectra used for these simulations and the LIDAR weighting function with fixed length, the shape of $|G_{v_{0L}v_0}|$ for different $\bar{v}$ will be similar over k, but different over f. The rotor effective wind speed v_0 is obtained from turbine data by a first-order-estimator using (21a) and (22a) similar to

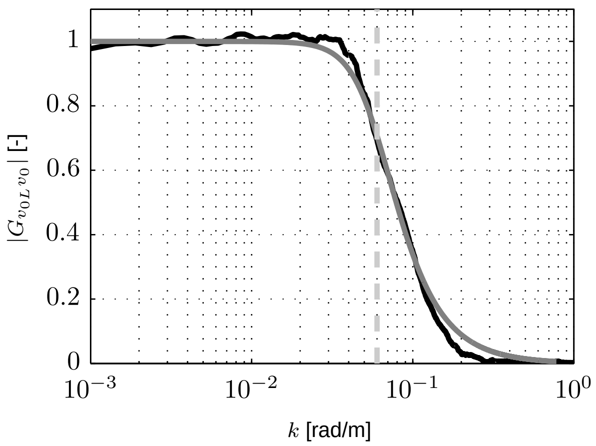

Figure 8: Black: Magnitude of the transfer function $|G_{v_{0L}v_0}|$ for a $1\ \mathrm{h}$ simulation. Dark gray: Fitted filter. Light gray: maximum wavenumber $\hat{k}$.

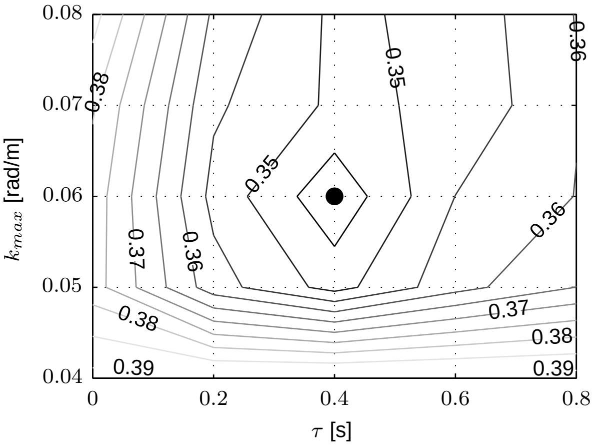

Figure 9: Percentage of $\sigma(\Omega)$ depending on τ and $\hat{k}$ compared to the baseline controller.

the one presented in [17] and v_{0L} from the LIDAR simulator presented above. Due to its low pass behaviour, the transfer function is modeled by

$$G_{v_{0L}v_0} = G_{Filter}\ e^{(T_{\text{Preview}} - T_{Filter} - \tau)s}, \tag{32}$$

where G_{Filter} is a second order Butterworth filter with a filter delay T_{Filter} averaged over the frequencies below the cut-off frequency $f_{\text{cutoff}} = \frac{\hat{k}\bar{v}}{2\pi}$ determined by a maximum wavenumber $\hat{k}$. The time τ compensates small errors in the model reduction (see [5]).

To prove the model, the same $1\ \mathrm{h}$ simulation is repeated with different $\hat{k}$ and τ, see Figure 9. The minimum in the standard deviation $\sigma(\Omega)$ of the rotor speed is found as expected at $\hat{k} = 0.06\ \mathrm{rad/m}$ and $\tau = 0.4\ \mathrm{s}$.

5 LIDAR Assisted Speed Control

The main goal of generator torque based speed control for variable speed wind turbines is to maximize the electrical power extraction below rated wind speed [19]. Therefore the turbine has to operate in the optimal aerodynamic range, hence at the optimal angle of attack at the rotor blades. This angle is represented by the ratio λ (27c) of the blade tip speed and the undisturbed rotor effective wind v_0. The electrical power P_{el} below rated wind speed than can be modeled as

$$P_{el} = \underbrace{\frac{1}{2}\rho\pi R^2 v_0^3}_{P_0} c_P(\lambda)\eta, \tag{33}$$

where ρ is the air density, P_0 the power of the undisturbed wind, η the efficiency of the electro-mechanical energy conversion and $c_P(\lambda)$ the power coefficient, representing the aerodynamic-mechanical energy conversion depending below rated wind speed only on λ. The relation of the power coefficient and λ depends on the rotor design and is shown for the used $5\,\mathrm{MW}$ turbine model in Figure 10(a). The control goal to operate at the aerodynamic optimum can be refined to track the optimal tip speed λ_{opt} by adjusting the generator torque M_g. This section shows how tracking λ_{opt} can be improved by using the knowledge of the incoming wind and why, nonetheless, it cannot be recommended.

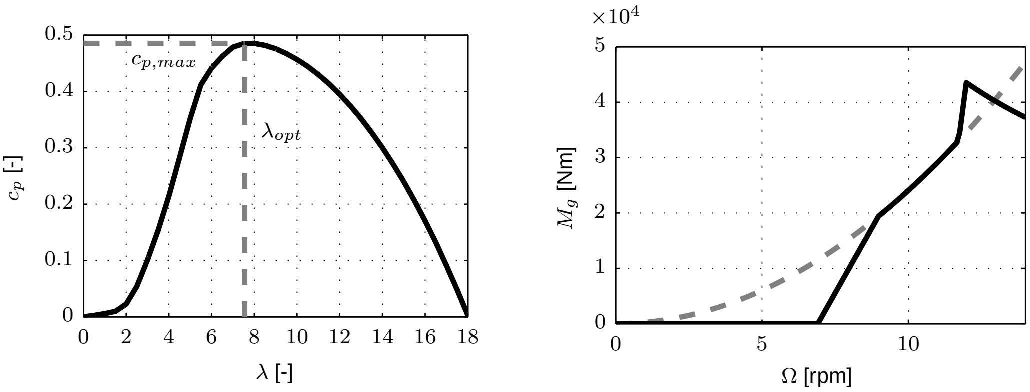

(a) (b)

Figure 10: (a) power coefficient c_P over tip speed ratio λ and (b) optimal relation of rotor speed and generator torque (dashed), used state feedback (solid) for the used turbine.

5.1 Indirect Speed Control

The particularity of controlling λ is the high nonlinearity of the control task and that λ is not available under normal circumstances. Therefore a common output feedback controller such as PI-controller cannot be applied. Normally nonlinear state feedback controllers are used, measuring the generator or rotor speed.

For derivations of state feedback control laws, the following nonlinear reduced model of a turbine is chosen according to [14]: where M_a is the aerodynamic torque, i the gear box ratio and J is the sum of the moments of inertia about the rotation axis.

In steady state, the generator torque maintaining λ_{opt} can be determined by using (27) and (27c):

$$M_{g,ISC}(\Omega) = \frac{1}{2}\rho\pi R^5 \frac{c_{p,max}}{\lambda_{opt}^3} i\Omega^2, \tag{34}$$

where all parameters are fixed, apart from the rotor speed. This equation is known as indirect speed control (ISC) and is normally applied for variable speed turbines.

Figure 10(b) shows the ISC [16], modified for transition from startup and to full load. The intersection of the state feedback law (solid) and the optimal, squared relation (dashed) is called ”Region 2”.

5.2 Direct Speed Control

By the LIDAR technology λ becomes measurable and therefore the proposed controller is considered as direct speed control (DSC). More details can be found in [3].
The basic idea of the proposed DSC is to keep the ISC and to find a feed forward update to compensate changes in the wind speed similar to the one used for collective pitch control [2]. Therefore the error ε is introduced

$$\varepsilon = \Omega - \Omega_{opt}, \tag{35}$$

where the optimal rotor speed Ω_{opt} is defined as

$$\Omega_{opt} = \frac{\lambda_{opt} v_0}{R}. \tag{36}$$

Using (25) and (36), the dynamic of the error ε can be described by:

$$\dot{\varepsilon} = \dot{\Omega} - \dot{\Omega}_{opt} = \frac{1}{J}(M_a(\Omega, v_0) - M_g/i) - \frac{\lambda_{opt}}{R}\dot{v}_0. \tag{37}$$

With the proposed DSC

$$M_{g,DSC}(\Omega) = M_{g,ISC} - \underbrace{iJ\frac{\lambda_{opt}}{R}\dot{v}_0(\Omega)}_{M_{g,FF}} \tag{38}$$

the error dynamic is

$$\begin{aligned} \dot{\varepsilon}_{DSC} &= \frac{1}{J}(M_a(\Omega, v_0) - M_{g,ISC}/i) \\ &= \frac{1}{2}\rho\pi R^5 (\frac{c_p(\lambda)}{\lambda^3} - \frac{c_{p,max}}{\lambda_{opt}^3})\Omega^2. \end{aligned} \tag{39}$$

Similar to [20] it can be shown that $\dot{\varepsilon}_{DSC} < 0$ and $\varepsilon = 0$ as long as the tip speed ratio resides above a calculable lower limit. Therefore, in the nominal case, changes in the wind will be perfectly compensated by the feedforward part $M_{g,FF}$. For the non-nominal case, caused by inaccurate measurements or model uncertainties, the feedback part $M_{g,ISC}$ compensates deviations from optimal operation.

5.3 Simulation Results

To demonstrate the effect of wind gust tracking by the use of wind speed signals, a coherent gust (similar to [21], but with only $1\,\mathrm{m/s}$ amplitude) is applied to the reduced nonlinear system (25) of a $5\,\mathrm{MW}$ wind turbine and ISC and DSC are compared. As seen in Figure 11, ISC reacts to wind speed changes slowly as the rotor speed varies slowly. During the transition of the gust, the tip speed ratio departs from the optimum λ_{opt}, resulting in a suboptimal angle of attack at the rotor blades and thereby reducing power extraction from the wind. As opposed to this, feedforward based control, using a perfect wind speed signal, can indeed maintain the optimal operation of the turbine. However the generator torque M_g has to vary substantially to achieve the optimal lambda tracking and even is reaching negative values.
In a second step, a turbulent wind field with mean wind speed $\bar{u} = 9\,\mathrm{m/s}$ and a turbulence intensity of 10% is created by TurbSim [12]. The low turbulence level is chosen to remain in Region 2 during the $10\,\mathrm{min}$ simulation. As simulation environment the FAST code [13] using a variable speed $5\,\mathrm{MW}$ wind turbine model [16] is coupled to the LIDAR simulator presented in [1], using a circle trajectory, see Figure 4. A rotor effective wind speed covering the rotor plane is calculated, using the model v_0-α-δ_V (6) and filtered using the filter (32). In Figure 12 the lower power spectral density (PSD) of the tip speed ratio applying direct speed control can be observed most notably for frequencies below f_{cutoff}. Therefore the standard deviation $\sigma(\lambda)$ is significantly reduced (see Table 1). However there is only a marginal increase in the energy production E_{el}. For this estimation the differences in rotational energy stored in the rotor are taken into account. Damage equivalent loads (DEL) for the low-speed shaft torque M_{LSS} are calculated based on a rainflow counting (Wöhler exponent of 4, lifetime 20 years, reference number of cycles $2 * 10^6$) and show an increase of 34.7%.
In a third step, 33 simulations are performed by using turbulent wind fields (Weibull distribution with

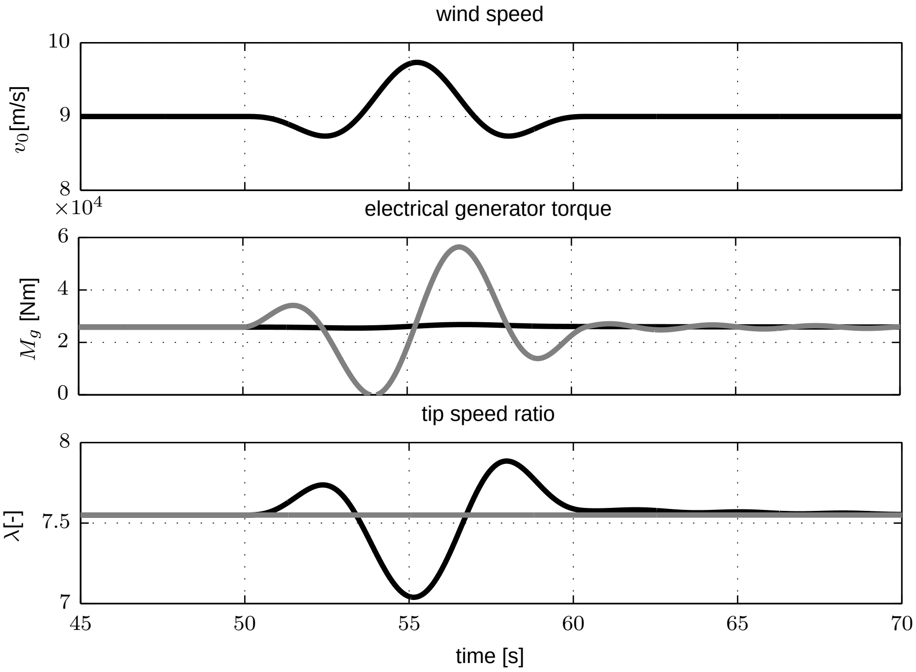

Figure 11: Reaction of the reduced model to a gust controlled by ISC (black) and DSC (gray).

$C = 10\,\mathrm{m/s}$, $k = 2$ and wind turbulence class A according to [21]). Bins of $2\,\mathrm{m/s}$ from 4 to $24\,\mathrm{m/s}$ are chosen, each simulated with 3 different seeds. The feedforward control algorithm is only applied if a wind within Region 2 is detected by the simulated LIDAR. Also for this extended evaluation the lifetime weighted standard deviation for Region 2 $\sigma_{R2}(\lambda)$ can be reduced. But the marginal increase in energy extraction of 0.09% is bought dearly by increasing loads affecting the whole drive train including rotor shaft, gear box, generator and bearings, represented by the low-speed shaft torque M_{LSS}, where the DEL rise up to 8.9% (see Table 2).

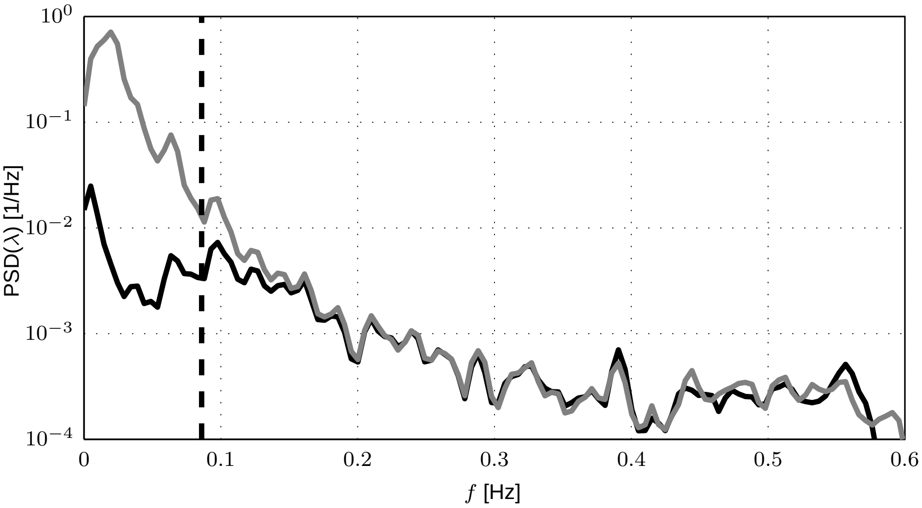

Figure 12: Power spectral density of the tip speed ratio: ISC (gray), DSC (black). Dashed: cutoff frequency of the wind speed filter.

	$\sigma(\lambda)$ [-]	E_{el} [kWh]	DEL(M_{LSS}) [MNm]
ISC	0.137	422.14	1.14
DSC	0.033	422.17	1.53
DSC/ISC [%]	24.1	100.01	134.7

Table 1: Comparison ISC and DSC for a $10\ \mathrm{min}$ simulation.

	$\sigma_{R2}(\lambda)$ [-]	E_{el} [GWh]	DEL(M_{LSS}) [MNm]
ISC	0.271	458.69	2.65
DSC	0.069	459.08	2.88
DSC/ISC [%]	25.6	100.09	108.9

Table 2: Life time comparison ISC and DSC.

5.4 Discussion

The fluctuation of the tip speed ratio can be used as a measure for the potential of energy optimization. Assuming the distribution of the tip speed ratio $\varphi_{\lambda_{opt};\sigma}$ to be Gaussian with mean λ_{opt} and a standard deviation $\sigma(\lambda)$, then the generated power can be estimated by

$$P_{el}(\sigma(\lambda)) = P_{el,max} \int_{-\infty}^{\infty} \varphi_{\lambda_{opt};\sigma(\lambda)} c_P(\lambda) d\lambda. \tag{40}$$

In Figure 13 this potential is quantified for the simulated wind turbine.

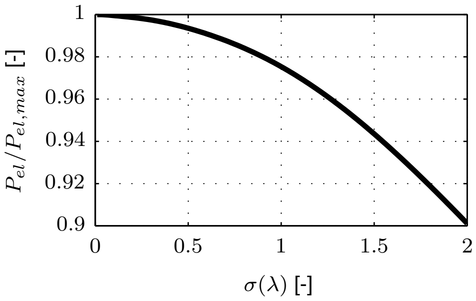

Figure 13: Relative power extraction by variation in tip speed ratio for the simulated turbine.

With (40) and the detected reduction of the tip speed ratio in Table 2 only an improvement in the energy production of 0.15% can be expected. Taking into account that by the given Weibull distribution, the turbine is only operating 19.0% of its lifetime in Region 2, this value is further reduced to 0.03%. The improvement of 0.09% in the energy production detected in the simulation is close to the expected value, considering the difficulty to detect such a small value.

Whereas the benefit of DSC should be irrelevant for all turbine sizes, the negative effect on loads should even increase for larger turbines due to the effect that the inertia J increases disproportionately.

6 Nonlinear Model Predictive Control

Model predictive control (MPC) is an advanced control tool, which predicts the future behavior of the system using an internal model and the current measurements. With this information the control actions necessary to regulate the plant are computed by solving an optimal control problem over a given time horizon. Part of the solution trajectory for the control inputs are transfered to the system, new measurements are gathered and the optimal control problem is solved again. Feedback is obtained, since the current state of the turbine is implemented as the initial condition of the optimal control problem.

The feedforward controller presented in the previous sections are updates to existing pitch and torque feedback controllers. In contrast the MPC is a control strategy which in the presented case controls pitch angle and generator torque independently from the common feedback controllers. This provides the possibility for further improvements, but also makes real applications more complex.

Here the basic principle and simulation results of a nonlinear model predictive control (NMPC) are presented. More details can be found in [4].

6.1 Controller Design

In this subsection a short overview of MPC is given, the optimal control problem is derived and then solved.

MPC can be categorized as either linear or nonlinear model predictive control. Linear MPC is based on linear models and is successfully applied in several industrial applications since the 1980s, mainly in chemical engineering [22]. However, many real systems have nonlinearities which cannot be neglected. Here NMPC often yields improved results by considering nonlinear models, objective functions and constraints.

There are several advantages of MPC in general. One is that it can handle multi-variable and non-quadratic (different number of inputs and outputs) control tasks naturally: additional control inputs or outputs will merely increase the number of optimization variables. Another advantage is that it considers actuator and system constraints during solving the optimal control problem. Furthermore, it provides a framework for incorporating a disturbance preview dynamically and tuning of MPC controllers is done intuitively by changing weights of a definable objective function. However, the main advantage of MPC is that it is in a mathematically sense an optimal controller. Solving the optimal control problem is not an easy task and several methods exist. Independent of the used method, the basic principle of model predictive control is illustrated in Figure 14 using piecewise constant parametrization: Future control action is planned to fulfill the control goal, e.g. reference signal tracking, considering a predicted disturbance.

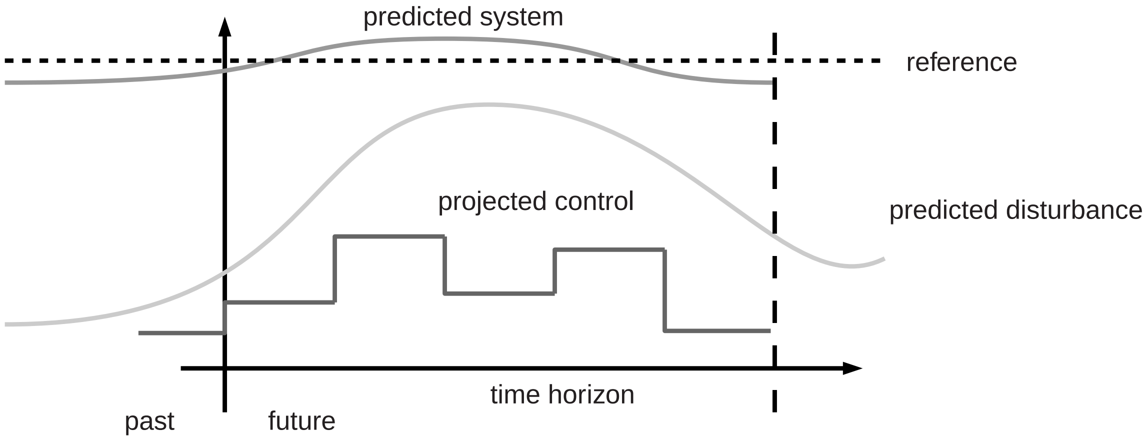

Figure 14: Principle of NMPC: Over a given time horizon the control action to a nonlinear system is optimized considering predicted disturbances to fulfill the control goals such as reference signal tracking.

6.1.1 Definition of the Optimal Control Problem

The considered optimal wind turbine control problem can be described by the following problem: The objective is to find the optimal control trajectory $u(\cdot)$ which minimizes the cost function J_{OCP}, which is defined as the integral over the time horizon T_f of the objective function F from the actual time t_0 to the final time $t_0 + T_f$, with the reduced nonlinear model and the set of constraints H.

$$\begin{aligned}
&\min_{u(\cdot)} J_{OCP} \\
\text{with: } & J_{OCP} = \int_{t_0}^{t_0+T_f} F(x(\tau), u(\tau), d(\tau))d\tau, \\
\text{s.t.: } & \dot{x} = f(x, u, d) \\
& x(t_0) = x_0 \\
& H(x(\tau), u(\tau), d(\tau)) \geq 0 \;\; \forall \tau \in [t_0, t_0 + T_f].
\end{aligned} \tag{41}$$

The crux of designing the NMPC is to translate the verbal formulation of the control goal to a mathematical formulation of F and H. In wind energy the overall goal of development can be stated very roughly as “minimizing energy production cost”. Such an optimization including the wind turbine design, manufacturing cost and operation can be found in [23]. However, for the optimal control problem the wind turbine is already designed and the optimal control goal can be stated very roughly as “maximizing energy production without damage during the lifetime of the turbine”, neglecting secondary requirements, e.g. noise limits. By classic wind turbine control [19] this is in general done by tracking optimal tip speed ratio below a certain wind speed defined as rated wind speed and by limiting rotor speed and power above the rated wind speed. This could be redefined for the NMPC, but special care has to be taken with NMPC characteristics. If for example the electrical power is directly maximized for wind speeds below rated wind speed by $F = (P_{el} - P_{rated})^2$ [24], the NMPC will slow down the turbine by increasing the generator torque, because this is optimal for the limited view of the NMPC, but evidently not for the overall energy production. In this work the optimal control problem is based on the classic interpretation of wind turbine control. The used objective function and constraints will be stated and explained here.

The objective function should be quadratic for numerical reasons (see Section 6.1.2). This requires the weights to be independent of the states x and inputs u, but are allowed to be dependent on the external disturbance d.

6.1.2 Solving the Optimal Control Problem

The optimal control problem is converted by the Direct Multiple Shooting method [22] into a nonlinear program. Here the control inputs are discretized in K piecewise constant stages. The ODEs of the model are solved numerically on each interval, starting in stage i with the initial values s_i for all states. The optimization is performed over the set of initial values and the control outputs. Additional constraints are applied to ensure that the states at the end of each stage coincide with the initial conditions of the subsequent stage. This method gives significant improvements over the Direct Single Shooting approach, especially with respect to numerical stability.

The resulting nonlinear program can be described as follows:

$$\begin{aligned}
&\min_{s_i, u_i} J_{NLP} \\
\text{with : } & J_{NLP} = \sum_{i=0}^{K-1} \int_{T_i}^{T_{i+1}} F(x_i(\tau; s_i, u_i), u_i, d(\tau))d\tau, \\
\text{s.t.} \forall i : \; & s_{i+1} - x_i(T_{i+1}; s_i, u_i) = 0 \\
& \dot{x}_i(\tau; s_i, u_i) = f(x_i(\tau; s_i, u_i), u_i, d(\tau)) \\
& H(x_i(\tau; s_i, u_i), u_i, d(\tau)) \geq 0 \;\; \forall \tau \in [T_i, T_{i+1}].
\end{aligned} \tag{42}$$

This nonlinear program can be solved iteratively with Sequential Quadratic Programming (SQP). The separation of the optimization problem into multiple stages results in a faster solution. This is caused by the better approximation of the Lagrangian Hessians of the nonlinear problem parts in each stage by low rank updates [25].

Here Omuses [25] is used, a front-end to the large-scale SQP-type nonlinear optimization solver HQP. The prediction horizon is chosen to $T_f = 10\,\mathrm{s}$ as a compromise between the different preview times of the LIDAR. The time steps are set equal to the LIDAR update rate $\Delta t_L = 0.2\,\mathrm{s}$, resulting in $K = T_f/\Delta t_L = 50$ stages. The differential equations are solved with a fourth order explicit Runge Kutta method.

The used control structure is depicted in Figure 16. A nonlinear estimator is used to estimate the tower dynamic states x_T and $\dot{x}_T$ and consists of a static nonlinear estimation of the aerodynamic thrust and a linear Luenberger estimator. To avoid resonance cases, notch filters (Butterworth, 2nd order) with stop band at $[0.9 f_{3P}, 1.1 f_{3P}]$ and $[0.9 f_0, 1.1 f_0]$ for y is used, where f_0 is the natural frequency of the tower. The number of control steps applied in a feedforward control to the system after each optimization is chosen to $K_{FF} = 1$. This implies that the optimization is repeated with new measurements each $0.2\,\mathrm{s}$ to close the control loop. The proof of closed loop stability of a nonlinear and constrained system solved by a model predictive controller is beyond the scope of this work and is quite complicated as J_{OCP} has to be a local Lyapunov function. There are some theoretical approaches [26] and practical recommendations [27], but the following results will show, that there is no stability problem in this case.

The NMPC controller needs the full state vector x_0 at the start of the optimization horizon. Only the rotor speed Ω, the tower fore-aft-acceleration $\ddot{x}_T$, the pitch angle θ and the pitch rate $\dot{\theta}$ can be considered as measurable signals. Therefore an estimator has to be implemented to reconstruct $\dot{x}_T$ and x_T.

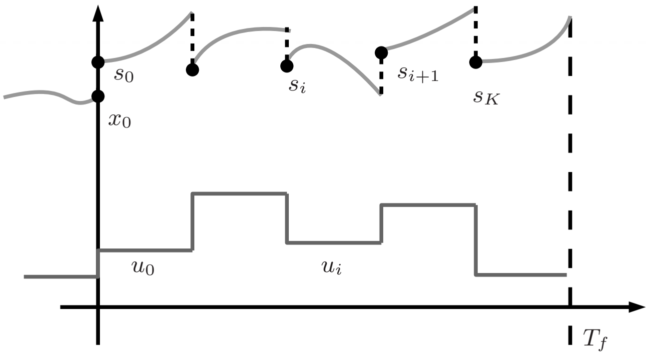

Figure 15: Principle of the direct multiple shooting method: x_0 is the initial point from the current measurement, s_i are the starting points for the nonlinear simulations which have to coincide with the final point of each simulation by changing the projected control imputs u_i over the K control steps up to the final time T_f.

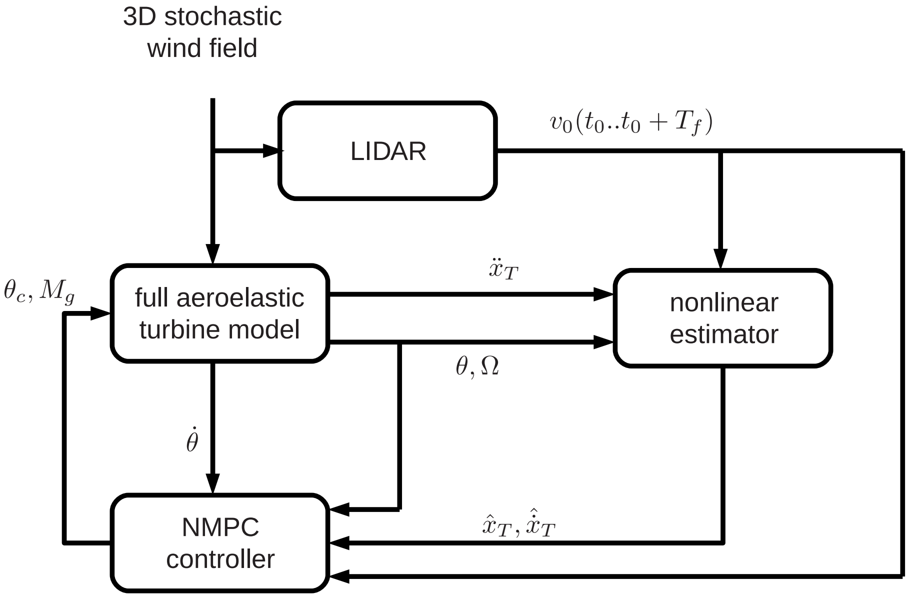

Figure 16: Closed loop NMPC.

6.2 Simulation Results

The most important benefits for the presented control may lie in the reduction of extreme loads in gust events. High load reduction can be also observed for fatigue loads. Both cases will be investigated in this subsection. A realistic reduction with the full aeroelastic model and simulated LIDAR measurements are shown for the extreme and subsequently for the fatigue loads. At the end of this section some considerations regarding the applicability of the NMPC in real time are presented. The NMPC is compared to the baseline controller [16] which has no information of the approaching wind.

6.2.1 Extreme Loads

In the time domain the different control strategies are compared with their reaction to gusts. Therefore hub-height time series are created with extreme operation gusts (EOG) according to current standards [21] at $v_{rated} + 2\ \mathrm{m/s} = 13.2\ \mathrm{m/s}$ and $v_{out} = 25\ \mathrm{m/s}$. Here the NMPC is used with the same parameters as in the detailed fatigue analysis (see Section 6.2.2). Figure 17 and Table 3 depict that with realistic conditions the load reduction is significant. Along with the wind speed the LIDAR estimation is plotted in the top part of Figure 17, which shows the spatial and temporal filtering effect depending on the wind speed of the LIDAR simulation: for low wind speeds the cut-off frequency of the applied filter (32) increases and the gust is smoothed by the measurement volume (18) and the applied filter.

	EOG $13.2\ \mathrm{m/s}$		EOG $25\ \mathrm{m/s}$	
	M_{yT} [MNm]	$\Delta\Omega$ [rpm]	M_{yT} [MNm]	$\Delta\Omega$ [rpm]
Baseline	129	2.34	99	3.01
NMPC	63	0.57	36	0.29
NMPC/Baseline [%]	49	24	36	10

Table 3: Maximum values of Figure 17.

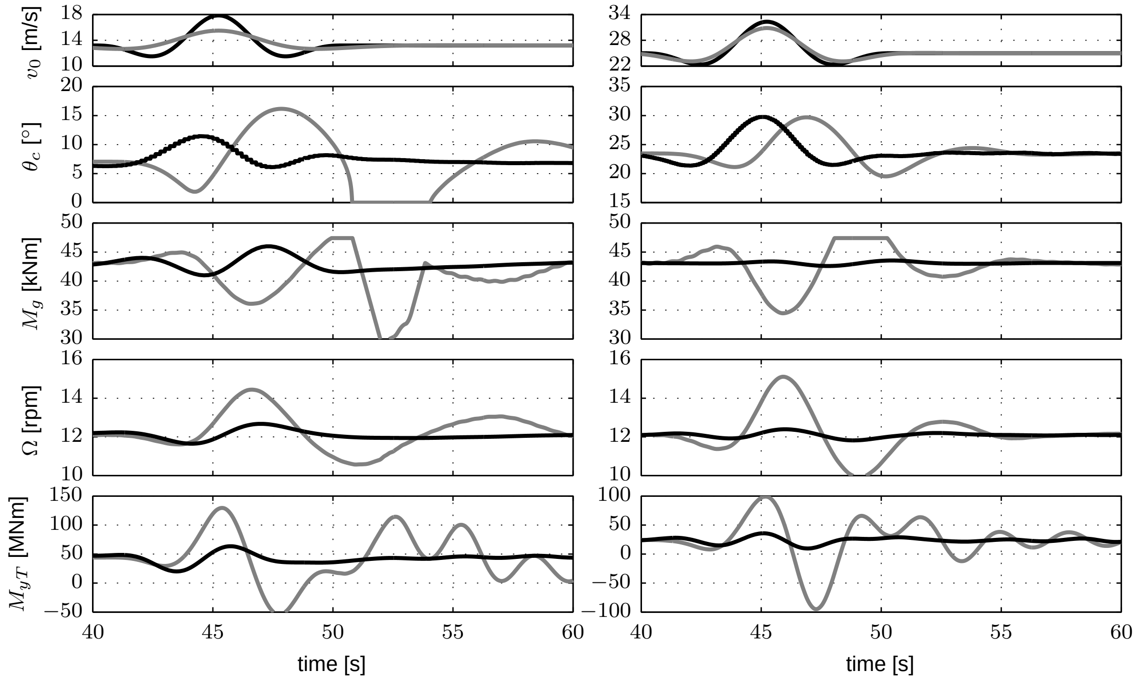

Figure 17: Simulation with aeroelastic model. Top: wind speed (black), LIDAR estimated rotor effective wind speed (gray). Below: pitch angle demand, generator torque, rotor speed and tower base fore-aft bending moment for baseline controller (gray) and NMPC (black).

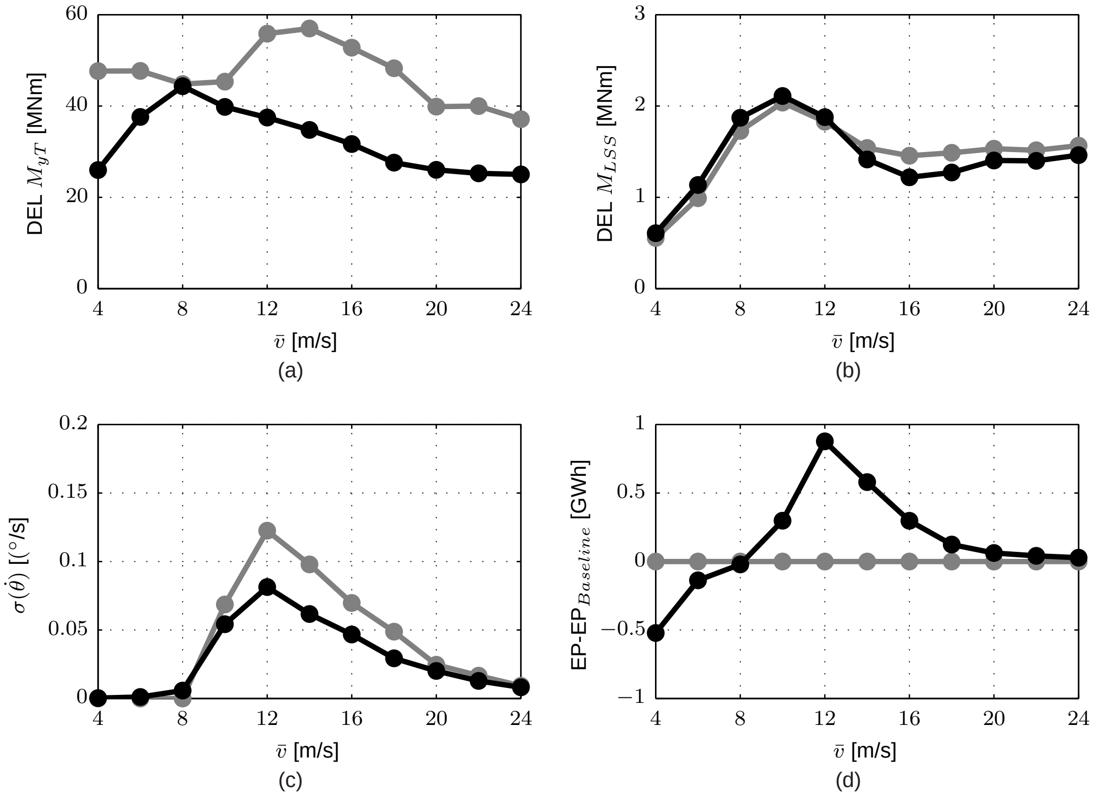

Figure 18: Distribution of lifetime weighted DEL of the tower base fore-aft bending moment (a) and the low-speed shaft torque (b), weighted standard deviation for pitch rate (c) and EP (d) for the baseline controller (gray) and NMPC (black) over the considered bins.

6.2.2 Fatigue Loads

To estimate the benefit for fatigue load reduction, various simulations with a set of turbulent TurbSim wind fields are conducted, featuring A-type turbulence intensity according to IEC 61400-1 [21] and a Rayleigh distribution with $C = 12\ \mathrm{m/s}$.

The NMPC coupled to the LIDAR simulator and the nonlinear estimator is tuned to have high load reduction on tower and blades together with low pitch activity and slightly improved energy production (EP). A larger power oscillation is tolerated in the partial load region.

Over all simulations the NMPC stabilizes the system and leads to satisfying control performance: Damage equivalent loads (DEL) are calculated based on a rainflow counting with Wöhler exponent of 4 and 10, typical for steel and composite material [28]. The distribution of the lifetime weighted DEL (20 years with Rayleigh distribution ($C = 12\ \mathrm{m/s}$), reference number of cycles $2 * 10^6$) of the tower base fore-aft bending moment and the low-speed shaft torque are shown in Figure 18(a) and 18(b), respectively. The loads for the tower are reduced not only for high wind speeds, but also for simulations with mean wind speeds of 4 and $6\ \mathrm{m/s}$ by limiting the rotor speed. Therefore less energy capture (see Figure 18(d)) is tolerated for these wind speeds. The loads on the low speed shaft are only reduced for high wind speeds.

For lower wind speeds the shaft loads are increased due to the improved λ_{opt}-tracking and limiting the rotor speed at lower wind speeds. The pitch activity (see Figure 18(c)) decreases for all wind bins except for $8\ \mathrm{m/s}$, where the slight increase is beneficial to achieve the optimization criteria.

Figure 19 and Table 4 summarize the results for all 33 simulations. For the LIDAR assisted NMPC the possible reduction of tower and blade DEL can be estimated to approximately 30 % and 10 %, respectively. The standard deviation of the pitch rate and the rotor speed are decreased to circa 30 % and 10 %. Furthermore, the energy production can be increased slightly by 0.30 %, but also the standard deviation of the power is increased by approximately 7 %.

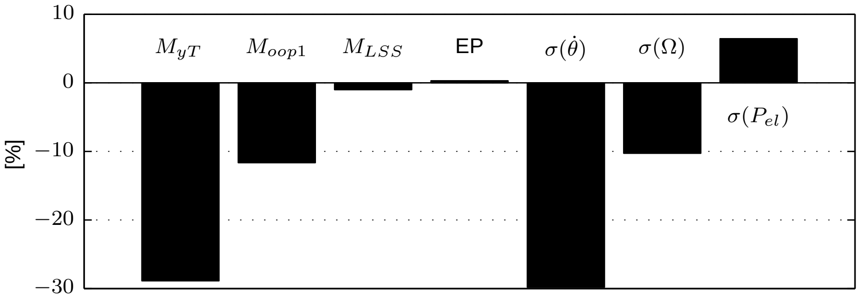

Figure 19: Overall improvement for the NMPC with respect to the baseline: Lifetime weighted DEL for tower base fore-aft bending moment M_{yT}, out-of-plane blade root bending moment of blade 1 M_{oop1} and low-speed shaft torque M_{LSS}, lifetime energy production, lifetime weighted standard deviation of pitch rate, rotor speed and electrical power.

	DEL(M_{yT}) [MNm]	DEL(M_{oop1}) [MNm]	DEL(M_{LSS}) [MNm]	EP [GWh]	$\sigma(\dot{\theta})$ [°/s]	$\sigma(\Omega)$ [rpm]	$\sigma(P_el)$ [MW]
Baseline	87.66	12.87	2.89	548.42	0.46	0.59	0.52
NMPC	62.35	11.37	2.87	550.05	0.32	0.53	0.55
NMPC/Baseline [%]	71.13	88.35	99.01	100.30	70.19	89.72	106.44

Table 4: Overall performance with $K = 50$ stages, repeating optimization after $K_{FF} = 1$ stage.

6.2.3 Considerations for Real Time Application

The NMPC previously presented was not capable of running in real time on the author's PC (single core 2.19 GHz). The $10\ \mathrm{min}$-simulations need approximately $1\ \mathrm{h}$ to run. It should be possible to reduce the computing time, e.g. by the usage of higher clock rate or improvement of the software communication, but the main issues for real time applications will remain. It is beyond the scope of this work to present an implementation which is applicable in real time. But some considerations and analysis will be presented in the remainder of this section. Two steps are introduced to reduce the time needed for the optimization below the allotted time: On the one side the computational effort is reduced and on the other side the allotted time is extended.

In the first step the computational effort to solve the nonlinear program (42) can be decreased by reducing the stages K. Here this is achieved by a shorter prediction horizon $T_f = 5.6\ \mathrm{s}$, resulting in $K = 28$ stages. In the second step the allotted time is extended by increasing the number of control steps $K_{FF} = 4$ applied to the system after each optimization. Table 4 summarize the results for the modified NMPC$_{RT}$. Compared to Table 4, the loads on the shaft increases as well as the standard deviation of the the rotor speed and the power. The standard deviation of the pitch rate can be further reduced. The new implementation has a small effect on the load reduction on the tower and blades.

This analysis shows that the aforementioned restrictions do not have a strong impact on the given implementation. Therefore the application of the presented approach on real systems is worth considering because a supervisory control could be designed which can switch to the baseline controller for the rare cases in which the solution is not found in the allotted time slot, improving the robustness of the control strategy. A supervisory control could also avoid applying suboptimal solutions of local minima, e.g. if the value of the cost function is far away from the range of previous minima.

	DEL(M_{yT}) [MNm]	DEL(M_{oop1}) [MNm]	DEL(M_{LSS}) [MNm]	EP [GWh]	$\sigma(\dot{\theta})$ [°/s]	$\sigma(\Omega)$ [rpm]	$\sigma(P_el)$ [MW]
Baseline	87.66	12.87	2.89	548.42	0.46	0.59	0.52
NMPC$_{RT}$	62.82	11.37	2.90	549.44	0.29	0.58	0.57
NMPC$_{RT}$/Baseline [%]	71.66	88.34	100.34	100.19	64.14	98.56	110.11

Table 5: Overall performance with $K = 28$ stages, repeating optimization after $K_{FF} = 4$ stages.

7 LIDAR Assisted Cyclic Pitch Control

The block diagram in Figure 20 illustrates the used feedforward control schema for the cyclic pitch control problem. More details can be found in [5] and [6]. The collective pitch controller (see Figure 7) is extended by two additional control loops: The flapwise blade root bending moments of the three blades M_{123} are transformed by the Coleman transformation T_c into a horizontal and vertical blade root bending moment, M_H and M_V, also considered as yaw and tilt moment. Those signals are feed back into two additional feedback controllers $\Sigma_{H,\text{FB}}$ and $\Sigma_{V,\text{FB}}$. Here standard PI controllers are used following [28]. The horizontal and vertical blade root bending moment M_H and M_V are mainly disturbed by the horizontal and vertical shear δ_H and δ_V. The horizontal and vertical shear can also be measured by a LIDAR system (see Section refsec:WindReconstruction). Those signals (δ_{HL} and δ_{VL}) can be used to calculate the feedforward updates $\theta_{H,\text{FF}}$ and $\theta_{H,\text{FF}}$ for the horizontal and vertical control loop. Here also static functions are proposed, which can be obtained from simulations or from modeling:

$$\begin{aligned}\theta_{H,\text{FF}} &= g_H \delta_{HL} \\ \theta_{V,\text{FF}} &= g_V \delta_{VL}\end{aligned} \tag{43}$$

Furthermore, the same filter 32 is used to avoid wrong pitch action. Also the time tracking issue is solved similar to the collective pitch feedforward controller: The feedforward update is added to the feedback with the prediction time τ before the shears reach the turbine, considering the time shift from the filter and the reconstruction method.

To demonstrate the benefit of LIDAR assisted cyclic pitch control, a collective pitch feedback only controller is compared to a cyclic pitch feedback only controller and a combined collective and cyclic feedback and feedforward controller. A wind field with mean wind speed $\bar{u} = 16\,\mathrm{m/s}$ and a turbulence intensity of 18% is used. Figure 21 shows the power spectral densities of pitch rate and out-of-plane blade root bending moment of blade 1. Both individual pitch controllers decrease variation of the blade root bending moment especially at the $1P$ frequency, but only the feedforward controller can reduce the loads around 0.1 Hz due to the collective feedforward part. Further investigations have to be done to investigate, whether similar load reduction can be obtained without the cyclic feedforward part. A validation of the LIDAR reconstructed rotor effective wind characteristics can be achieved by comparing to those estimated from turbine data. Figure 22 compares the shears obtained from model (6) with shears obtained by a zero-order estimation from blade root bending moment, showing as expected a better correlation for δ_V than for δ_H. Therefore further investigations have to be done to investigate, if the correlation between the LIDAR measurement and the turbine reaction regarding the shears is sufficient to use it for feedforward control.

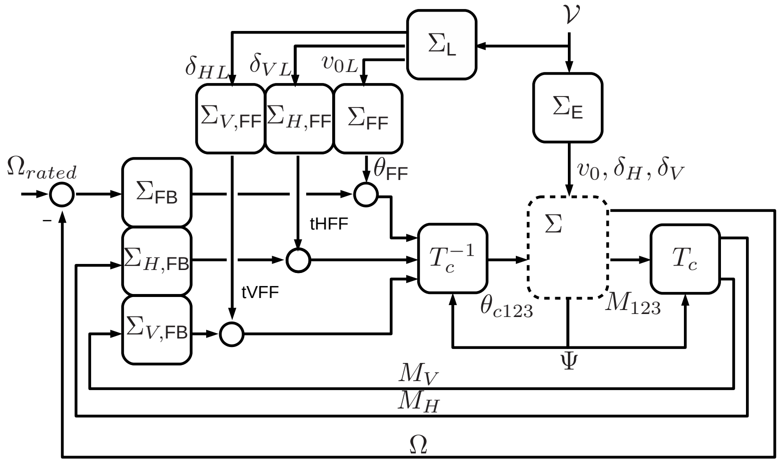

Figure 20: Cyclic pitch feedforward control: The feedforward controllers try to compensate the effects of the wind field $\mathcal{V}$ to the rotor speed Ω and the horizontal and vertical blade root bending moments, M_H and M_V.

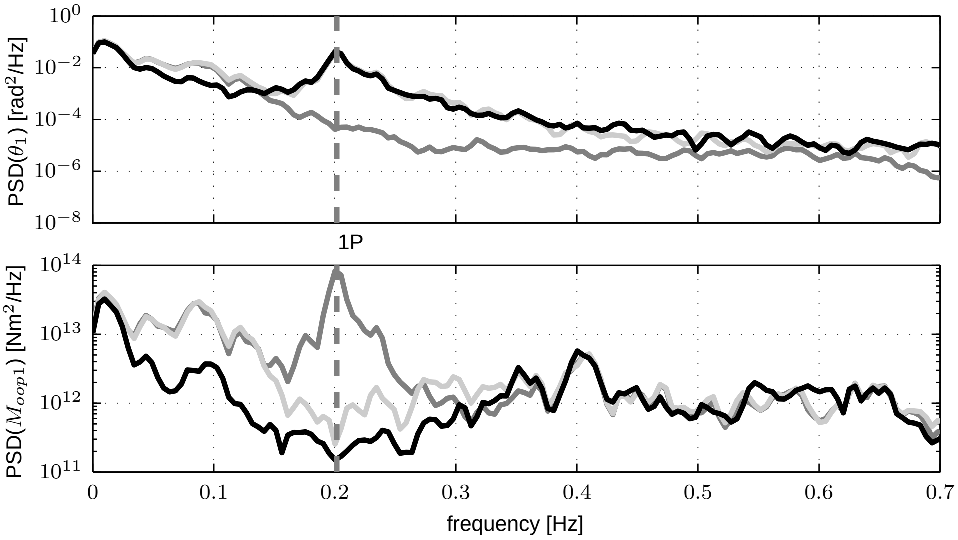

Figure 21: Power spectral density of pitch rate and out-of-plane blade root bending moment of blade 1: Collective pitch feedback only (dark gray), cyclic pitch feedback only (light gray) and combined collective and cyclic feedback and feedforward (black).

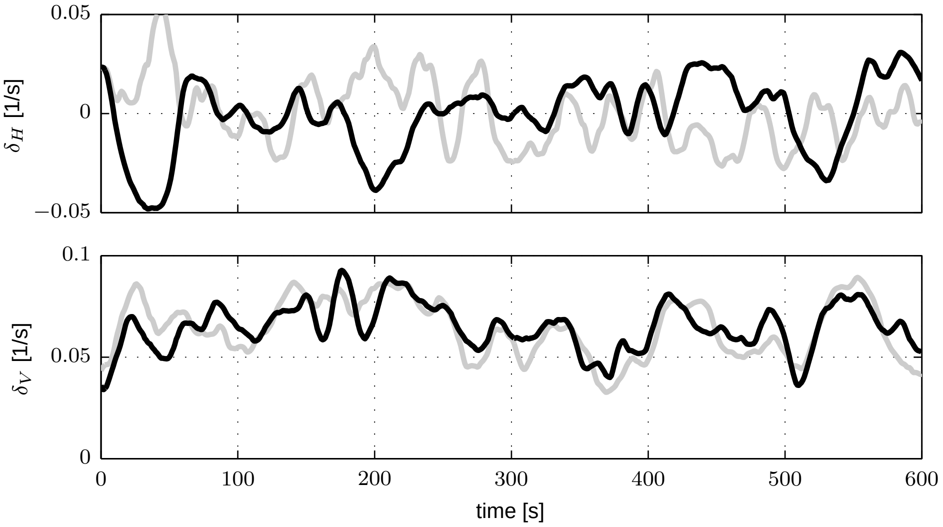

Figure 22: Estimated (1 min average) shears using LIDAR (black) and turbine data (gray).

8 LIDAR Assisted Yaw Control

Yaw control is usually done by active yaw control. Due to the large moment of inertia of the rotor about the yaw axis, the nacelle is aligned with the wind with slow rates and only, if the misalignment exceeds a certain value [29]. The demand signal is normally calculated from a nacelle mounted wind vane or sonic anemometer. There are mainly two disadvantages for these sensors: Firstly the signal is heavily disturbed for a operating turbine, e.g. by passing blades and therefore must be averaged over a certain time [19]. Secondly these sensors are measuring at one single point therefore are unable to detect changes over the rotor disc.

A nacelle mounted LIDAR system avoids these disadvantages, being able to measure the undisturbed inflow over the entire rotor area. Therefore using LIDAR technology has been proposed in literature for yaw control and the presented improvement in energy yield are promising and far exceed the estimated looses of 1 to 2% due to standard yaw control [29]. The first part of this section shows the capability and the problems of a simulated LIDAR system to capture the wind direction. In the second part data is analysed and finally in the third part the conditions for improvements in energy yield by LIDAR assisted yaw control are discussed theoretically. More details can be found in [3].

8.1 Simulation Using Generic Wind

The scope of the presented simulation study is to test if the methods presented in Section 2 are robust and can be applied to turbulent wind fields. This is not obvious, because the simulation model of the wind (here IEC Kaimal [21]) and of the LIDAR ((17) and (18)) are more complex than the used design wind (12) and LIDAR model (1). Similar work has been presented [30], using an empiric reconstruction method and Mann turbulence.

The 33 Class A wind fields from section 5 are generated with a horizontal mean flow angle of $\alpha_H = 10\,\mathrm{deg}$. The $10\,\mathrm{min}$-wind fields are scanned again with the mentioned LIDAR simulator, imitating the SWE-LIDAR system [7] using a Lissajous-like trajectory.Only the third measurement plane in $116\,\mathrm{m}$ is used, scanning a regular $87\,\mathrm{m}$ by $87\,\mathrm{m}$ grid with $n = 49$ focus points. The misalignment detected by the LIDAR $\hat{\alpha}_{HL}$ is estimated with the model (12) using those focus points from the last n points, where no impact with the turbine blades is simulated. Due to the positioning on top of the nacelle, similar to the one used in the experiment, this usually results in a loss of $\approx 30\%$.

The resulting $\hat{\alpha}_{HL}$ signal is very oscillating and for better illustration a $1\,\mathrm{min}$ running average is used in Figure 23. For comparison, the misalignment signal of a point measurement is plotted, which could be obtained from a sonic anemometer on hub height neglecting the disturbance of an operating turbine. Initially it seems that no advantage is gathered by the averaging over the rotor disc. But the reason for this effect can be observed in the running average of the effective horizontal shear from the wind field: The misalignment signal estimated with the LIDAR is disturbed by the horizontal shear, due to the effects described in Section 2.

However, Figure 24 shows that for all 33 simulations the error of the misalignment estimation in the $10\,\mathrm{min}$ mean is below $1\,\mathrm{deg}$ due to the fact that the mean of the effective horizontal shear for the wind field is close to zero. In the mean absolute error over the used 3 seeds a better estimation can be observed for higher wind speeds where the turbulence intensity of the wind fields is lower.

The results of this simulation study show that with the proposed method of wind reconstruction it is possible for a simulated LIDAR to estimate the misalignment of a turbine in the scale of $10\,\mathrm{min}$ similar to the simulated undisturbed sonic anemometer. An important requirement is that there is no constant horizontal shear, which is difficult to guarantee in complex terrain.

8.2 Simulation Using Real Data

From the simulation study above it is hard to estimate the improvement of LIDAR assisted yaw control compared to the standard yaw control: On one hand it is hard to model the disturbance which a nacelle mounted anemometer will experience in real conditions. On the other hand it is difficult to estimate the real wind direction in real experiments to evaluate the improvements.

Therefore, a simulation study is presented here using data from a real experiment: A scanning LIDAR system was developed and installed on a $5\,\mathrm{MW}$ wind turbine measuring the wind inflow. In the following investigation it is assumed that the LIDAR system is able to estimate the $10\,\mathrm{min}$ misalignment. This assumption is reasonable, considering the simulation study above and the location (flat terrain) where no constant horizontal shear is expected. Data sets of at least $4\,\mathrm{h}$ are selected from almost 5 months

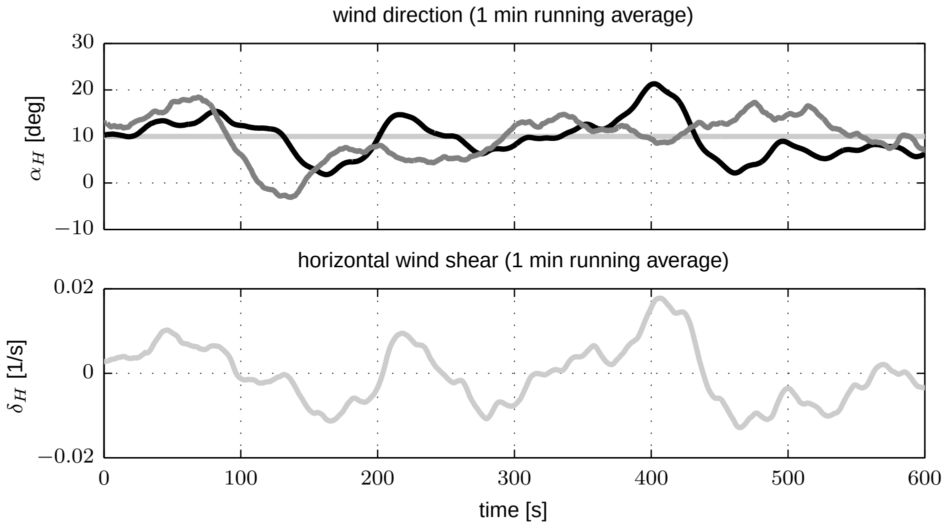

Figure 23: Misalignment and horizontal shear. From a wind field (light gray), LIDAR estimation (black) and sonic anemometer simulation (dark gray).

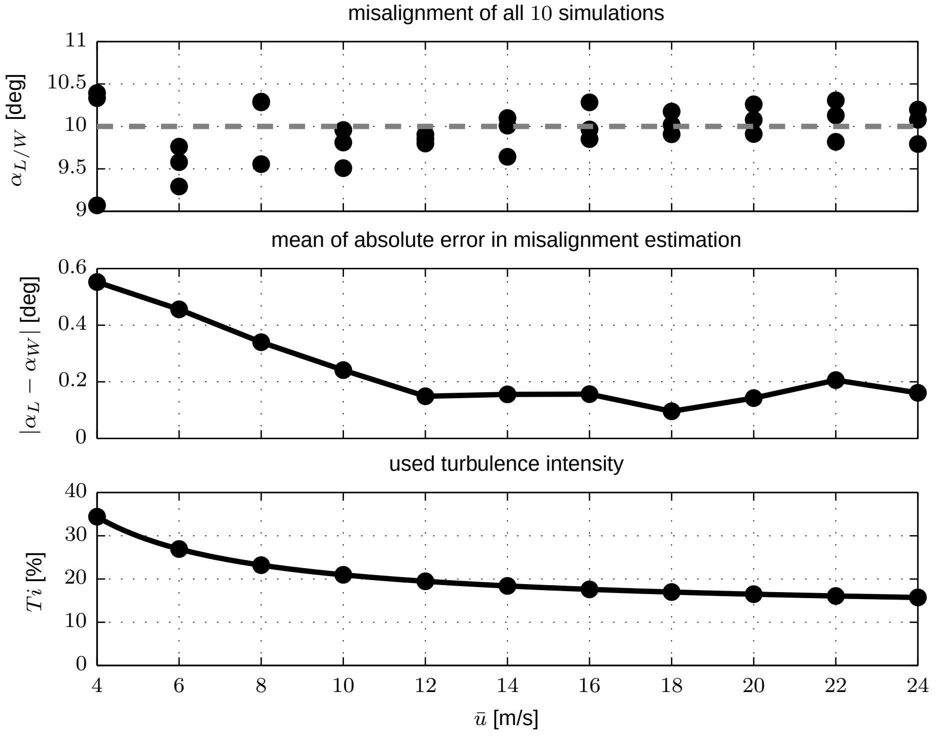

Figure 24: Evaluation of the simulation study for all 33 simulations.

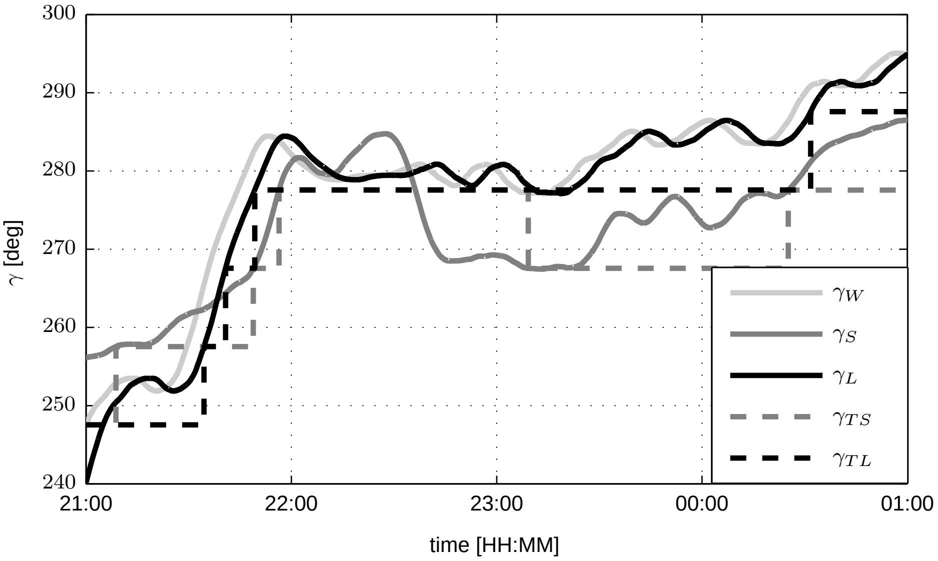

Figure 25: Measured wind directions and simulated yaw positions.

of measurement using only data with Lissajous-like trajectory and 50% of data availibility and data with the turbine in normal operation. By this procedure a total of $223\,\mathrm{h}$ is analyzed and the misalignment detected by the LIDAR $\hat{\alpha}_{HL}$ is again estimated using model (12).

In a first step the overall average is calculated: in the period of the $223\,\mathrm{h}$ an average misalignment of only $0.7\,\mathrm{deg}$ is detected. This shows, that no significant static misalignment can be detected. But this number is no indication, whether LIDAR assisted yaw control can reduce the fluctuation of the misalignment.

Therefore the basic idea of the second step is to analyze, how the wind direction tracking can be improved by the LIDAR compared to the sonic anemometer if the same yaw control strategy is applied, and if the LIDAR is able to perfectly estimate the misalignment. Therefore the absolute yaw direction signal γ_T is superposed with the relative, $10\,\mathrm{min}$ averaged misalignment signals from the nacelle mounted LIDAR and sonic anemometer to the absolute wind direction signals γ_L and γ_S from LIDAR and sonic anemometer, respectively. The assumed real wind direction γ is equal to γ_L, but $5\,\mathrm{min}$ shifted back in time, due to the assumption of the perfect LIDAR measurement and the delay of a $10\,\mathrm{min}$ average. Then following yaw control [29] is applied to γ_L and γ_S: The turbine yaws, if the absolute $10\,\mathrm{min}$ averaged misalignment is above $10\,\mathrm{deg}$. Starting for both instruments with no misalignment, the simulated turbine directions γ_{TL} and γ_{TS} are obtained. Figure 25 shows an extreme example of this method for better illustration.

With this method it can be simulated, how the turbine would have been yawed for both instruments. Finally, the resulting yaw misalignment for both instruments can be calculated by comparing the simulated turbine positions with the wind direction:

$$\begin{aligned}\alpha_{HL} &= \gamma - \gamma_{TL}\\ \alpha_{HS} &= \gamma - \gamma_{TS}.\end{aligned} \tag{44}$$

Due to the average time and the threshold in the control strategy, the difference in the fluctuation of both signals over the $223\,\mathrm{h}$ of data is relatively low: In this case the sonic anemometer assisted yaw control would have been achieved a standard deviation of $\sigma(\alpha_{HS}) = 6.4\,\mathrm{deg}$ and the LIDAR assisted yaw control despite of the perfect measurement a standard deviation of $\sigma(\alpha_{HS}) = 4.1\,\mathrm{deg}$.

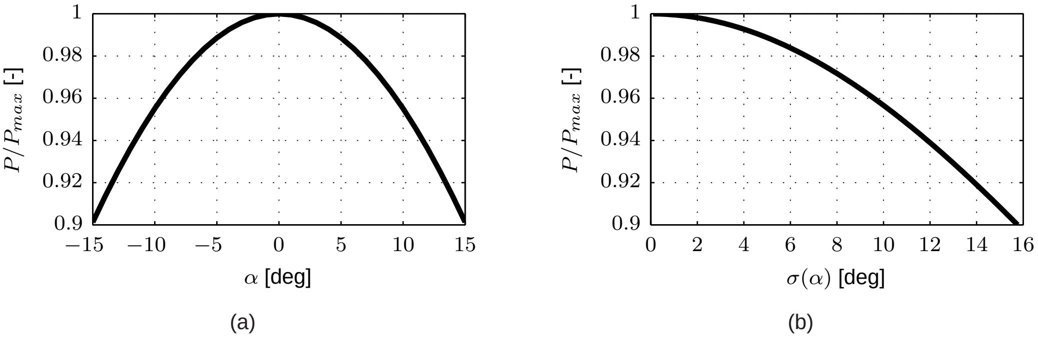

Figure 26: Power loss due to static (a) and dynamic (b) misalignment.

8.3 Discussion

Both studies above show, the yaw misalignment can be divided in a static and a dynamic subproblem. In reality there will be a mixture of both, but this perception is helpful to rate the benefits which can be achieved by using a LIDAR system for yaw control.

If there is a static misalignment $\bar{\alpha}_H$, the loss in power can be modeled as [19]:

$$P_{el}(\bar{\alpha}_H) = P_{el,max}\cos^3(\bar{\alpha}_H). \tag{45}$$

Figure 26(a), shows e.g. that $\approx 10\%$ of power is lost, if the turbine is misaligned by $\approx 15\,\mathrm{deg}$ to one side. This value can be considered as a lower bound, because a misalignment in full load operation will not have an effect on the power. Such a static misalignment could be caused by a miscalibrated anemometer or if the hub height wind direction has an offset compared to the rotor effective wind direction due to a very inhomogenious inflow e.g. in complex terrain. A static misalignment can be solved by better calibration of the standard nacelle anemometer and does not need a constant use of a LIDAR system. In the case of investigated data the detected static misalignment of $0.7\,\mathrm{deg}$ only would cause a power loss of 0.02%. This low value can be due to the fact that the considered turbine is a well calibrated prototype in flat terrain.

A constant use of a nacelle mounted LIDAR system is justified, if the fluctuation of yaw misalignment can be reduced. Similar to the discussion in Section 5.4 the misalignment can be assumed to be Gaussian distributed with zero mean and a standard deviation $\sigma(\alpha_H)$. Then the loss in power can be modeled by:

$$P_{el}(\sigma(\alpha_H)) = P_{el,max}\int_{-\infty}^{\infty}\varphi_{0;\sigma(\alpha_H)}\cos^3(\alpha_H)d\alpha_H. \tag{46}$$

The loss in power due to the dynamic misalignment is plotted in Figure 26(b) and again is only applicable to partial load operation. The reduction of $\sigma(\alpha_H)$ and therefore an improvement of the power output is limited to the control strategy: a reduction to $0\,\mathrm{deg}$ would require immediate yawing of the rotor which is neither feasible nor reasonable due to the induced loads. In the presented investigation a reduction from $6.4\,\mathrm{deg}$ to $4.1\,\mathrm{deg}$ yield to an improvement from $99.3\% - 98.2\% = 1.1\%$ using (46). This low value despite of assumed perfect reconstruction of the alignment by the LIDAR system can be due to the location but still gives an estimation of improvement which can be expected.

9 Conclusion and Outlook

In this work a method is presented to reconstruct wind characteristics based on LIDAR measurements and shortcomings are shown. This method is used in various approaches to increase the energy production and to reduce loads of wind turbines: Collective pitch feedforward control and direct speed control uses the knowledge of the incoming wind speed to calculate a control update to existing feedback controllers. Collective pitch feedforward control is a promising strategy to reduce extreme and fatigue loads. Filtering the LIDAR signal is an important issues, because not all turbulences can be measured. With the direct speed control only marginal benefit can be gained. This is due to the fact that the standard variable speed control is already close to the aerodynamic optimum. The approach of the Nonlinear Model Predictive Control differs from the feedforward approaches: the future behavior of a wind turbine is optimized by solving an optimal control problem repetitively using the wind speed preview adjusting simultaneously the pitch angle and the generator torque. Therefore loads on tower, blades and shaft cab be further reduced especially for for wind conditions near rated wind speed. Further load reduction of the blades can be gained with cyclic pitch feedforward control, extending the feedforward approach to reduce also tilt and yaw moments of the rotor. Another approach uses the wind direction estimation by a LIDAR system for yaw control. Here an increase of energy production by a couple of percent can be expected, depending on the control strategy and the inhomogeneity of the wind.

Acknowledgment

This research is funded by the German Federal Ministry for the Environment, Nature Conservation and Nuclear Safety (BMU) in the framework of the German joint research project ”LIDAR II - Development of nacelle-based LIDAR technology for performance measurement and control of wind turbines” (FKZ 0325216B). Thanks all the people getting the LIDAR systems and the different measurement campaigns working, special thanks to the Andreas Rettenmeier, Martin Hofsß̈, Jan Anger, Ines Wr̈th and Oliver Bischoff of the SWE Lidar group, my supervisors Po Wen Cheng, Martin Kühn and Lucy Pao and my students Valeria Basterra, Paul Brodbeck, Patrick Grau, Florian Haizmann, Stefan Kapp, Timo Maul and David Trabucchi. Thanks to Björn Siegmeier from AREVA Wind GmbH for his help and the access to the turbine measurement data.

References

[1] D. Schlipf, J. J. Trujillo, V. Basterra, and M. Kühn, “Development of a wind turbine LIDAR simulator,” in *Proc. EWEC*, 2009.

[2] D. Schlipf, T. Fischer, C. E. Carcangiu, M. Rossetti, and E. Bossanyi, “Load analysis of look-ahead collective pitch control using LiDAR,” in *Proc. DEWEK*, 2010.

[3] D. Schlipf, S. Kapp, J. Anger, O. Bischoff, M. Hofsäß, A. Rettenmeier, U. Smolka, and M. Kühn, “Prospects of optimization of energy production by LiDAR assisted control of wind turbines,” in *Presentation at EWEA*, 2011.

[4] D. Schlipf, D. J. Schlipf, and M. Kühn, “Nonlinear model predictive control of wind turbines using LIDAR,” *Accepted for Wind Energy Journal*, 2012.

[5] F. Dunne, D. Schlipf, L. Y. Pao, A. D. Wright, B. Jonkman, N. Kelley, and E. Simley, “Comparison of two independent lidar-based pitch control designs,” in *Proc. 50th AIAA Aerospace Sciences Meeting Including the New Horizons Forum and Aerospace Exposition*, 2012.

[6] D. Schlipf, D. Trabucchi, O. Bischoff, M. Hofsäß, J. Mann, T. Mikkelsen, A. Rettenmeier, J. J. Trujillo, and M. Kühn, “Testing of frozen turbulence hypothesis for wind turbine applications with a scanning LIDAR system,” in *Proc. ISARS*, 2010.

[7] A. Rettenmeier, O. Bischoff, M. Hofsäß, D. Schlipf, J. J. Trujillo, and M. Kühn, “Wind field analyses using a nacelle-based lidar system,” in *Presentation at EWEC*, 2010.

[8] T. Mikkelsen, J. Mann, M. Courtney, and M. Sjöholm, “Windscanner: 3-d wind and turbulence measurements from three steerable doppler lidars,” *IOP Conference Series: Earth and Environmental Science*, vol. 1, no. 1, p. 012018, 2008. [Online]. Available: http://stacks.iop.org/1755-1315/1/i=1/a=012018

[9] A. Rettenmeier, O. Bischoff, D. Schlipf, J. Anger, M. Hofsäß, P. W. Cheng, R. Wagner, M. Courtney, and J. Mann, “Turbulence and wind speed investigations using a nacelle-based lidar scanner and a met mast,” in *Presentation at the EWEA*, 2012.

[10] J. P. Cariou, “Pulsed lidars,” in *Remote Sensing for Wind Energy. Risøreport Risø-I-3184(EN)*. A. Peña and C. B. Hasager, June 2011, pp. 65–81, risø-DTU.

[11] P. Lindelöw, “Fiber based coherent lidars for remote wind sensing,” Ph.D. dissertation, Technical University of Denmark, 2008.

[12] J. Jonkman and M. L. Buhl, “TurbSim user’s guide,” NREL, Tech. Rep. NREL/TP-500-41136, April 2007.

[13] ——, “FAST user’s guide,” NREL, Tech. Rep. NREL/EL-500-38230, August 2005.

[14] C. L. Bottasso, A. Croce, B. Savini, W. Sirchi, and L. Trainelli, “Aero-servo-elastic modelling and control of wind turbines using finite-element multibody procedures,” *Multibody Syst. Dyn.*, vol. 16, pp. 291–308, 2006.

[15] R. Gasch, J. Twele, and P. Bade, *Windkraftanlagen: Grundlagen, Entwurf, Planung und Betrieb*. Teubner, 2005.

[16] J. Jonkman, S. Butterfield, W. Musial, and G. Scott, “Definition of a 5-mw reference wind turbine for offshore system development,” *Technical Report NREL/TP-500-38060*, 2009.

[17] E. van der Hooft and T. G. van Engelen, “Estimated wind speed feed forward control for wind turbine operation optimization,” *European Wind Energy Conference, London*, vol. 1, p. 9, 2004.

[18] S. Schuler, D. Schlipf, M. Kühn, and F. Allgöwer, “ℓ_1-optimal multivariable pitch control for load reduction on large wind turbines,” in *Proc. EWEC*, 2010.

[19] T. Burton, D. Sharpe, N. Jenkins, and E. Bossanyi, *Wind Energy Handbook*. John Wiley & Sons, 2001.

[20] K. Johnson, L. Pao, M. Balas, and L. Fingersh, “Control of variable-speed wind turbines,” *IEEE Control Systems Magazine*, vol. 06, pp. 70–81, 2006.

[21] *IEC 61400-1 third edition 2005-08 Wind turbines - Part 1: Design requirements*, IEC Std., Rev. third edition, 2005.

[22] R. Findeisen, “Nonlinear model predictive control: A sampled-data feedback perspective,” Ph.D. dissertation, Universität Stuttgart, 2005.

[23] C. L. Bottasso, F. Campagnolo, and A. Croce, “Computational procedures for the multi-disciplinary constrained optimization of wind turbines,” Dipartimento di Ingegneria Aerospaziale, Politecnico di Milano, Milano, Italy, Scientific Report DIA-SR 10-02, 2010.

[24] L. C. Henriksen, “Model predictive control of wind turbines,” Ph.D. dissertation, Technical University of Denmark, 2011.

[25] R. Franke, “Omuses - a tool for the optimization of multistage systems and hqp a solver for sparse nonlinear optimization,” TU Ilmenau, Technical report, 1998.

[26] D. Q. Mayne, J. B. Rawlings, C. V. Rao, and P. O. M. Scokaert, “Constrained model predictive control: Stability and optimality,” *Automatica*, vol. 36, pp. 789–814, 2000.

[27] H. Chen and F. Allgöwer, “A quasi-infinite horizon nonlinear model predictive control scheme with guaranteed stability,” *Automatica*, vol. 34, pp. 1205–1217, 1998.

[28] E. Bossanyi, B. Savini, M. Iribas, M. Hau, B. Fischer, D. Schlipf, T. van Engelen, M. Rossetti, and C. E. Carcangiu, “Advanced controller research for multi-mw wind turbines in the upwind project,” *Wind Energy*, vol. 15, no. 1, pp. 119–145, 2012.

[29] E. Hau, *Windkraftanlagen*, 4th ed. Springer, 2008.

[30] A. Kragh, M. Hansen, and T. Mikkelsen, “Improving yaw alignment using spinner based LIDAR,” in *Proc. 49th AIAA Aerospace Sciences Meeting Including the New Horizons Forum and Aerospace Exposition*, 2011.